

SmoQyDQMC.jl: A flexible implementation of determinant quantum Monte Carlo for Hubbard and electron-phonon interactions (version 2.0 release)

Benjamin Cohen-Stead^{1,2} , Sohan Malikaruge Costa^{1,2} , James Neuhaus^{1,2} , Andy Tanjeroon Ly^{1,2} , Yutan Zhang³ , Richard Scalettar³ , Kipton Barros⁴ , and Steven Johnston^{1,2,*} 

1 Department of Physics and Astronomy, The University of Tennessee, Knoxville, Tennessee 37996, USA

2 Institute for Advanced Materials and Manufacturing, The University of Tennessee, Knoxville, Tennessee 37996, USA

3 Department of Physics and Astronomy, University of California, Davis, California 95616, USA

4 Theoretical Division and CNLS, Los Alamos National Laboratory, Los Alamos, New Mexico 87545, USA

* sjohn145@utk.edu

January 27, 2026

Abstract

We introduce version 2.0 of the `SmoQyDQMC.jl` package, a Julia implementation of the determinant quantum Monte Carlo algorithm. `SmoQyDQMC.jl` supports generalized tight-binding Hamiltonians with local and extended Hubbard and generalized electron-phonon (*e*-*ph*) interactions, including non-linear *e*-*ph* coupling and anharmonic lattice potentials. Our implementation uses an optimized hybrid Monte Carlo method with exact forces to efficiently sample the phonon fields, enabling the simulation of low-energy phonon branches, including acoustic phonons. The `SmoQyDQMC.jl` package also uses a flexible scripting interface, allowing users to adapt it to different workflows and interface with other software packages in the Julia ecosystem. The code for this package can be downloaded from our GitHub repository at <https://github.com/SmoQySuite/SmoQyDQMC.jl> or installed using the Julia package manager. The online documentation, including examples, is found at <https://smoqysuite.github.io/SmoQyDQMC.jl/stable/>.

Contents

1	Introduction	2
1.1	Overview & Scope	2
1.2	Background and Motivation	3
1.3	Relevant Links, Documentation, and Reporting	4
2	Supported Hamiltonians	5
2.1	Specifications	5
2.2	A Flexible Approach to Electron-Phonon Coupling	7
3	Algorithm Details	7

3.1	Formulation of DQMC Algorithm	7
3.2	DQMC Simulation Overview	11
3.3	Single-Particle Electron Green's Functions	11
3.4	Numerically Stable Framework for DQMC Simulations	13
3.5	The Checkerboard Approximation	17
3.6	Twisted Boundary Conditions	19
3.7	Efficient Local Updates of Hubbard-Stratonovich Fields	20
3.8	HMC Updates of Phonon Fields	21
3.8.1	Evaluating the Derivative of the Action	23
3.8.2	Resolving Disparate Timescales in the Bosonic Action	24
3.9	Reflection, Swap and Radial Updates	25
3.10	Error Estimation and Reweighting	27
3.11	Chemical Potential Tuning	28
4	Performance	29
5	Summary & Future Directions	30
A	Supported Hubbard-Stratonovich Transformations	31
A.1	Hubbard Interaction Hubbard-Stratonovich (HS) Transformations	31
A.1.1	Hubbard Spin-Channel Hirsch HS Transformation	31
A.1.2	Hubbard Spin-Channel Gauss-Hermite HS Transformation	32
A.1.3	Hubbard Density-Channel Hirsch HS Transformation	32
A.1.4	Hubbard Density-Channel Gauss-Hermite HS Transformation	32
A.2	Extended Hubbard Interaction Hubbard-Stratonovich (HS) Transformations	32
A.2.1	Extended Hubbard Spin-Channel Hirsch HS Transformation	32
A.2.2	Extended Hubbard Density-Channel Gauss-Hermite HS Transformation	33
A.3	Hubbard-Stratonovich (HS) Transformation Selection Guidance	33
B	Numerical Stabilization Routines	33
B.1	Routine for Stable Left Matrix Multiply	33
B.2	Routine for Stable Right Matrix Multiply	34
B.3	Routine for Stable Evaluation of Eq. (41)	34
B.4	Routine for Stable Evaluation of Eq. (43)	34
B.5	Routine for Stable Evaluation of Eq. (47b) and Eq. (48b)	34
References		34

1 Introduction

1.1 Overview & Scope

This paper introduces version 2.0 of [SmoQyDQMC.jl](#), a user-friendly Julia implementation of the determinant quantum Monte Carlo (DQMC) algorithm [1, 2], and its associated auxiliary packages.¹ The [SmoQyDQMC.jl](#) package is capable of simulating a broad class of tight-

¹The names for both the [SmoQyDQMC.jl](#) package, and the overarching SmoQy Suite GitHub organization it lives in, are inspired by the Great Smoky Mountain range running along the Tennessee–North Carolina border in the southeastern United States.

binding Hamiltonians with local and extended Hubbard and/or generalized electron-phonon (e -ph) interactions. Model Hamiltonians can be defined on arbitrary lattice geometries and a wide variety of measurements can be performed in simulations, including density-density, spin-spin, bond-bond, and current-current correlation functions and pairing for different symmetries. The code has been designed with a scripting interface inspired by packages like `ITensor.jl` [3], rather than a configuration file-based workflow commonly found in other open-source implementations of DQMC [4, 5]. This design allows users to easily incorporate `SmoQyDQMC.jl` into complex workflows and directly interface it with the Julia programming language's rich ecosystem of scientific computing and machine learning packages. Crucially, our implementation accomplishes this flexibility without sacrificing performance, with `SmoQyDQMC.jl` achieving ideal $O(\beta N^3)$ scaling in computational complexity in the system size N and inverse temperature β .

This document provides detailed descriptions of `SmoQyDQMC.jl`'s design philosophy and underlying algorithms, including changes made in the 2.0 release. It is also intended to serve as a citeable document when using this code for research. This document is not intended to serve as a detailed user manual for the package. Instead, we encourage readers to consult our online [documentation](#), which will be maintained as a living document with new examples and reference material added continuously over the package's lifetime.

1.2 Background and Motivation

Quantum Monte Carlo (QMC) algorithms are a powerful family of methods for performing numerically exact nonperturbative simulations of quantum many-body systems. These methods have been successfully applied in many different fields of physical science, ranging from lattice gauge theory [6, 7] and nuclear physics work [8, 9], to quantum chemistry [10, 11] and, our focus here, condensed matter physics research [12–42]. These methods come in many flavors, including zero temperature projection and variational Monte Carlo methods, to finite-temperature auxiliary field methods like DQMC or continuous-time QMC and beyond.

DQMC is an auxiliary-field QMC method [1, 2], which calculates expectation values of a quantum system within the grand canonical ensemble. The method has been applied to a broad class of problems in condensed matter physics, including single- [2, 43–52] and multi-band Hubbard models [53–59], negative- U models [60–63], e -ph coupled Hamiltonians like the Holstein [64–68] and Su-Schrieffer-Heeger (SSH) models [69–74] and their strongly correlated counterparts [75–78], and topological systems [79–84]. It has also been used to simulate ultra-cold atom experiments [85–90], quantum entanglement [91–93] and beyond [94–97].

Several open-source implementations of the DQMC algorithm have been developed over the years with support for different classes of Hamiltonians. Perhaps the most popular and well-known are the *Algorithms for Lattice Fermions* (ALF) [5] and *QUantum Electron Simulation Toolbox* (QUEST) [4] projects. The QUEST package supports single- and multi-orbital Hubbard Hamiltonians defined on arbitrary lattice geometries. The ALF package provides support for a much broader class of Fermionic interactions, as well as coupling to classical or quantum bosonic fields, which enables simulations of standard e -ph Hamiltonians like the Holstein model. Both QUEST and ALF are currently implemented in Fortran90, which hinders their integration with modern machine learning and scientific computing packages; however, PyALF [98], a high-level python wrapper for ALF, is available.

The `SmoQyDQMC.jl` package is a Julia implementation of the DQMC algorithm, with support for tight-binding Hubbard Hamiltonians with and without e -ph interactions. The code leverages hybrid Monte Carlo (HMC) methods [99–103] to sample the phonon fields, which allows it to treat a much broader class of e -ph interactions. The package also includes additional features that are useful in various DQMC applications, but are not commonly available. Specifically, this package includes support for

1. arbitrary lattices and bases in zero-, one-, two-, and three-dimensions;
2. intra- and inter-orbital Hubbard interactions in any site/orbital in the lattice, as well as extended Hubbard interactions;
3. real or complex hopping parameters, including twisted boundary conditions, to enable the introduction of magnetic fields or mitigate finite size effects;
4. Hamiltonians with spin-dependent tight-binding and e - ph interaction parameters;
5. momentum-dependent e - ph interactions, including long-range Holstein- and SSH-like couplings;
6. coupling to multiple phonon branches, either via the same or different microscopic coupling mechanisms;
7. low-energy optical and acoustic phonon branches;
8. nonlinear e - ph interactions and anharmonic lattice potentials up to fourth order in the atomic displacements;
9. dynamical tuning of the chemical potential to archive a targeted density $\langle n \rangle$;
10. spatial disorder in any Hamiltonian parameter; and
11. support for measuring a wide range of common observables on arbitrary lattice geometries.

Importantly, `SmoQyDQMC.jl` is user friendly and utilizes a scripting interface rather than more traditional workflows based on input configuration files. This design allows users to implement straightforward parallelization at the script level, adapt the package to their existing workflows, and more readily interface `SmoQyDQMC.jl` with the rich ecosystem of scientific computing packages being actively developed in the Julia programming language. For example, it can be readily coupled to existing machine learning and artificial intelligence packages to enable new research in this direction [104–106].

If the `SmoQyDQMC.jl` package is unable to meet the needs of a particular user, we have also released two lower-level supporting packages to expedite the development of custom implementations. The first package, `JDQMCFrameworks.jl`, implements the core computational kernel of the DQMC algorithm. The second package, `JDQMCMeasurements.jl`, implements a set of functions for measuring various correlation functions for arbitrary lattice geometries in a DQMC simulation. This package also exports several additional utility functions for transforming measurements from position space to momentum space, and also measuring susceptibilities by integrating correlation functions over the imaginary time axis. These two lower-level packages were used to develop the `SmoQyDQMC.jl` package, and provide the tools necessary for a user to develop their own specialized implementations of the DQMC algorithm.

1.3 Relevant Links, Documentation, and Reporting

The source code for the `SmoQyDQMC.jl` package and its associated auxiliary packages can be found on the [SmoQy Suite's GitHub page](#) [107]. As a package registered with Julia programming language's [General registry](#), the package can also be installed using the Julia package manager by issuing the command

```
julia> ]
pkg> add SmoQyDQMC
```

The package's documentation, including examples, can be found in the [online documentation](#) [108]. It includes a full API and a growing list of example scripts that can be used to run simulations of different model Hamiltonians. The source code for the `JDQMCFrameworks.jl` [109] and `JDQMCMeasurements.jl` [110] packages can also be found on the SmoQy Suite's GitHub page.

2 Supported Hamiltonians

2.1 Specifications

This section describes the class of Hamiltonians currently supported by the [SmoQyDQMC.jl](#) package, and how the various terms appearing in the Hamiltonian are parameterized within the code base. Throughout this section, we use bold roman indices (e.g., $\mathbf{i}, \mathbf{j}, \dots$) to index the unit cells within a cluster, and Greek symbols (e.g., ν, γ, μ, \dots) to index the different atomic orbitals and phonon modes within each unit cell. We also normalize $\hbar = 1$ and denote $\mathcal{N} = N \cdot n$ ($\mathcal{N}_{\text{ph}} = N \cdot n_{\text{ph}}$) as the total number of orbitals (phonon modes) in the lattice, where N is the number of unit cells, and n (n_{ph}) is the number of orbitals (phonon modes) per unit cell.

For our purposes, it is convenient to partition the full Hamiltonian into three terms

$$\hat{\mathcal{H}} = \hat{\mathcal{U}} + \hat{\mathcal{K}} + \hat{\mathcal{V}}, \quad (1)$$

where $\hat{\mathcal{U}}$ describes the non-interacting lattice (phonon) degrees of freedom and $\hat{\mathcal{K}}$ and $\hat{\mathcal{V}}$ are the total electron kinetic and potential energies, respectively. Note that both $\hat{\mathcal{K}}$ and $\hat{\mathcal{V}}$ can depend on the dynamical lattice coordinates, leading to an e -ph coupling that is either diagonal or off-diagonal in the orbital basis. $\hat{\mathcal{V}}$ also includes any contributions from local intra- and inter-orbital Hubbard repulsion or extended Hubbard interactions.

The non-interacting lattice terms are further subdivided into the sum of three terms

$$\hat{\mathcal{U}} = \hat{\mathcal{U}}_{\text{qho}} + \hat{\mathcal{U}}_{\text{anh}} + \hat{\mathcal{U}}_{\text{disp}}. \quad (2)$$

The first term

$$\hat{\mathcal{U}}_{\text{qho}} = \sum_{\mathbf{i}, \nu} \left[\frac{1}{2M_{\mathbf{i}, \nu}} \hat{P}_{\mathbf{i}, \nu}^2 + \frac{1}{2} M_{\mathbf{i}, \nu} \Omega_{0, \mathbf{i}, \nu}^2 \hat{X}_{\mathbf{i}, \nu}^2 \right] \quad (3)$$

describes the placement of local quantum harmonic oscillator (QHO) modes in a cluster, i.e. an Einstein solid, while the second term

$$\hat{\mathcal{U}}_{\text{anh}} = \sum_{\mathbf{i}, \nu} \left[\frac{1}{24} M_{\mathbf{i}, \nu} \Omega_{a, \mathbf{i}, \nu}^2 \hat{X}_{\mathbf{i}, \nu}^4 \right] \quad (4)$$

introduces anharmonic contributions to the oscillator potential. The third term

$$\hat{\mathcal{U}}_{\text{disp}} = \sum_{\substack{\mathbf{i}, \nu \\ \mathbf{j}, \gamma}} \frac{M_{\mathbf{i}, \nu} M_{\mathbf{j}, \gamma}}{M_{\mathbf{i}, \nu} + M_{\mathbf{j}, \gamma}} \left[\tilde{\Omega}_{0, (\mathbf{i}, \nu), (\mathbf{j}, \gamma)}^2 (\hat{X}_{\mathbf{i}, \nu} - \hat{X}_{\mathbf{j}, \gamma})^2 + \frac{1}{12} \tilde{\Omega}_{a, (\mathbf{i}, \nu), (\mathbf{j}, \gamma)}^2 (\hat{X}_{\mathbf{i}, \nu} - \hat{X}_{\mathbf{j}, \gamma})^4 \right] \quad (5)$$

introduces coupling (or dispersion) between the QHO modes. The sums over \mathbf{i} (\mathbf{j}) and ν (γ) run over unit cells in the lattice and phonon modes within each unit cell.

The position and momentum operators for each QHO mode are $\hat{X}_{\mathbf{i}, \nu}$ and $\hat{P}_{\mathbf{i}, \nu}$ respectively, with corresponding phonon mass $M_{\mathbf{i}, \nu}$. The spring constant is $K_{\mathbf{i}, \nu} = M_{\mathbf{i}, \nu} \Omega_{0, \mathbf{i}, \nu}^2$, with $\Omega_{0, \mathbf{i}, \nu}$ specifying the phonon frequency. $\hat{\mathcal{U}}_{\text{anh}}$ then introduces an anharmonic $\hat{X}_{\mathbf{i}, \nu}^4$ contribution to the QHO potential energy that is controlled by the parameter $\Omega_{a, \mathbf{i}, \nu}$. Similarly, $\tilde{\Omega}_{0, (\mathbf{i}, \nu), (\mathbf{j}, \gamma)}$ ($\tilde{\Omega}_{a, (\mathbf{i}, \nu), (\mathbf{j}, \gamma)}$) is the coefficient controlling harmonic (anharmonic) dispersion between QHO modes. Note that unlike harmonic parameters $\Omega_{0, \mathbf{i}, \nu}$ and $\tilde{\Omega}_{0, (\mathbf{i}, \nu), (\mathbf{j}, \gamma)}$, the anharmonic parameters $\Omega_{a, \mathbf{i}, \nu}$ and $\tilde{\Omega}_{a, (\mathbf{i}, \nu), (\mathbf{j}, \gamma)}$ do not have units of frequency, but instead include an additional factor of inverse length squared.

The electron kinetic energy is conveniently expressed as

$$\hat{\mathcal{K}} = \hat{\mathcal{K}}_0 + \hat{\mathcal{K}}_{\text{ssh}} = \sum_{\sigma} \hat{\mathcal{K}}_{0,\sigma} + \sum_{\sigma} \hat{\mathcal{K}}_{\text{ssh},\sigma}. \quad (6)$$

The first term describes the non-interacting spin- σ electron kinetic energy

$$\hat{\mathcal{K}}_{0,\sigma} = - \sum_{\substack{\mathbf{i}, \nu \\ \mathbf{j}, \gamma}} \left[t_{\sigma,(\mathbf{i},\nu),(\mathbf{j},\gamma)} \hat{c}_{\sigma,\mathbf{i},\nu}^{\dagger} \hat{c}_{\sigma,\mathbf{j},\gamma} + \text{h.c.} \right], \quad (7)$$

where $t_{\sigma,(\mathbf{i},\nu),(\mathbf{j},\gamma)}$ is the spin- σ hopping integral from orbital γ in unit cell \mathbf{j} to orbital ν in unit cell \mathbf{i} , and may be real or complex. The second term describes the interaction between the lattice degrees of freedom and the spin- σ electron kinetic energy via a Su-Schrieffer-Heeger (SSH)-like coupling mechanism [111, 112]

$$\hat{\mathcal{K}}_{\text{ssh},\sigma} = \sum_{\substack{\mathbf{i}, \nu, \eta \\ \mathbf{j}, \gamma, \rho}} \sum_{m=1}^4 (\hat{X}_{\mathbf{i},\nu} - \hat{X}_{\mathbf{j},\gamma})^m \left[\alpha_{\sigma,m,(\mathbf{i},\nu,\eta),(\mathbf{j},\gamma,\rho)} \hat{c}_{\sigma,\mathbf{i},\eta}^{\dagger} \hat{c}_{\sigma,\mathbf{j},\rho} + \text{h.c.} \right]. \quad (8)$$

Here, the modulations of the spin- σ hopping integrals to m^{th} ($= 1 - 4$) order in displacement are controlled by the parameters $\alpha_{\sigma,m,(\mathbf{i},\nu,\eta),(\mathbf{j},\gamma,\rho)}$. Note that if the corresponding bare hopping amplitude $t_{\sigma,(\mathbf{i},\eta),(\mathbf{j},\rho)}$ is complex, then the $\alpha_{\sigma,m,(\mathbf{i},\nu,\eta),(\mathbf{j},\gamma,\rho)}$ parameter is defined to share the same complex phase. This convention ensures that $e\text{-ph}$ interaction defined in Eq. (8) only modulates the magnitude of the hopping amplitude and not the phase.

Lastly, the electron potential energy is expressed as

$$\hat{\mathcal{V}} = \hat{\mathcal{V}}_0 + \hat{\mathcal{V}}_{\text{hol}} + \hat{\mathcal{V}}_{\text{hub}} + \hat{\mathcal{V}}_{\text{exh}} = \sum_{\sigma} \hat{\mathcal{V}}_{0,\sigma} + \sum_{\sigma} \hat{\mathcal{V}}_{\text{hol},\sigma} + \hat{\mathcal{V}}_{\text{hub}} + \hat{\mathcal{V}}_{\text{exh}}, \quad (9)$$

where

$$\hat{\mathcal{V}}_{0,\sigma} = \sum_{\mathbf{i}, \nu} [(\epsilon_{\sigma,\mathbf{i},\nu} - \mu_{\sigma}) \hat{n}_{\sigma,\mathbf{i},\nu}] \quad (10)$$

is the non-interacting spin- σ electron potential energy. Here, μ_{σ} is the spin- σ chemical potential and $\epsilon_{\sigma,\mathbf{i},\nu}$ is the spin- σ on-site energy for orbital ν in unit cell \mathbf{i} .

The second term

$$\hat{\mathcal{V}}_{\text{hol},\sigma} = \begin{cases} \sum_{\mathbf{j}, \gamma} \left[\sum_{m=1,3} \kappa_{\sigma,m,(\mathbf{i},\nu),(\mathbf{j},\gamma)} \hat{X}_{\mathbf{i},\nu}^m (\hat{n}_{\sigma,\mathbf{j},\gamma} - \frac{1}{2}) + \sum_{m=2,4} \kappa_{\sigma,m,(\mathbf{i},\nu),(\mathbf{j},\gamma)} \hat{X}_{\mathbf{i},\nu}^m \hat{n}_{\sigma,\mathbf{j},\gamma} \right] \\ \sum_{\mathbf{j}, \gamma} \sum_{m=1}^4 \kappa_{\sigma,m,(\mathbf{i},\nu),(\mathbf{j},\gamma)} \hat{X}_{\mathbf{i},\nu}^m \hat{n}_{\sigma,\mathbf{j},\gamma} \end{cases} \quad (11)$$

is the contribution to the spin- σ electron potential energy that results from a Holstein- or Fröhlich-like coupling to the lattice degrees of freedom. The parameter $\kappa_{\sigma,m,(\mathbf{i},\nu),(\mathbf{j},\gamma)}$ controls the strength of this coupling in the $\hat{\mathcal{V}}_{\text{hol},\sigma}$ term. It is important to note that the two parametrizations shown in Eq. (11) that are available in [SmoQyDQMC.jl](#) are inequivalent, with the first being particle-hole symmetric in the atomic limit.

The third term

$$\hat{\mathcal{V}}_{\text{hub}} = \begin{cases} \sum_{\mathbf{i}, \nu} U_{\mathbf{i},\nu} (\hat{n}_{\uparrow,\mathbf{i},\nu} - \frac{1}{2}) (\hat{n}_{\downarrow,\mathbf{i},\nu} - \frac{1}{2}) \\ \sum_{\mathbf{i}, \nu} U_{\mathbf{i},\nu} \hat{n}_{\uparrow,\mathbf{i},\nu} \hat{n}_{\downarrow,\mathbf{i},\nu} \end{cases} \quad (12)$$

defines the intra-orbital/local Hubbard interaction, where $U_{i,\nu}$ is the interaction strength. Note that `SmoQyDQMC.jl` allows the user to parameterize the Hubbard interaction using either functional form for \hat{V}_{hub} . The top-most is particle-hole symmetric and is often useful at half-filling.

Lastly, the fourth term

$$\hat{V}_{\text{exh}} = \begin{cases} \sum_{i,\nu,\sigma} V_{(i,\nu),(j,\gamma)} (\hat{n}_{\sigma,i,\nu} - \frac{1}{2})(\hat{n}_{\sigma',j,\gamma} - \frac{1}{2}) \\ \sum_{i,\nu,\sigma} V_{(i,\nu),(j,\gamma)} \hat{n}_{\sigma,i,\nu} \hat{n}_{\sigma',j,\gamma} \end{cases} \quad (13)$$

introduces extended Hubbard interactions with $V_{(i,\nu),(j,\gamma)}$ subject to the constraint $V_{(i,\nu),(i,\nu)} = 0$. Note, however, that local inter-orbital Hubbard interactions can still be treated using Eq. (13) by defining an interaction within a single unit cell $i = j$ between a pair of orbitals $\nu \neq \gamma$ that share the same basis vector $\mathbf{r}_\nu = \mathbf{r}_\gamma$. In this case, the parameter $V_{(i,\nu),(j,\gamma)}$ is typically denoted $U_{i,\nu,\gamma}$. As with the local Hubbard interaction, users can parameterize the extended Hubbard interaction using either a particle-hole symmetric (top) or asymmetric (bottom) form.

2.2 A Flexible Approach to Electron-Phonon Coupling

The class of Hamiltonians supported by `SmoQyDQMC.jl` is flexible enough to accommodate the simulation of most standard e - ph model Hamiltonians. For example, the canonical single-band Holstein model with coupling to a single Einstein phonon branch can be obtained by placing a QHO mode in each unit cell and setting $\hat{U}_{\text{anh}} = \hat{U}_{\text{disp}} = \hat{K}_{\text{ssh}} = 0$, while retaining the \hat{V}_{hol} term [113]. Similarly, extended Holstein or Fröhlich models can be treated with suitably chosen $\kappa_{\sigma,m,(i,\nu),(i,\gamma)}$ values [114, 115]. The optical single-band SSH model in D -dimensions [72] can be arrived at by setting $\hat{U}_{\text{anh}} = \hat{U}_{\text{disp}} = \hat{V}_{\text{hol}} = 0$ but requires D QHO modes per unit cell. The bond SSH model can also be expressed by coupling pairs of QHO modes, one with finite mass and the other with infinite mass, effectively associating the finite mass QHO mode with a bond [72, 116]. The acoustic SSH model can be expressed by introducing QHO modes with zero frequency ($\Omega_{0,i,\nu} = 0$), that are then coupled together with the \hat{U}_{disp} term [112]. Importantly, `SmoQyDQMC.jl` allows users to define Hamiltonians that combine these various models, enabling the simulation of systems with multiple phonon branches that can each couple to the electrons in different ways.

3 Algorithm Details

This section provides details on the various algorithms used in the `SmoQyDQMC.jl` package. Here, we have taken an axiomatic approach and focused on describing what the algorithms do rather than providing detailed derivations or justifications for their correctness. Instead, we have provided several references throughout the text for any reader who is interested in the relevant derivations.

3.1 Formulation of DQMC Algorithm

DQMC is an auxiliary field QMC method for simulating systems of itinerant fermions on a lattice in the grand canonical ensemble [1, 2]. For an inverse temperature $\beta = 1/T$ ($k_B = 1$), the algorithm adopts a discrete imaginary time grid $\tau = \Delta\tau \cdot l$, where $l = 1, \dots, L_\tau$ indexes the imaginary time-slice and $\Delta\tau = \beta/L_\tau$. Using this grid, DQMC then expresses the partition function as a path-integral in imaginary time

$$\mathcal{Z} = \text{Tr}[\hat{B}^{L_\tau}], \quad (14)$$

where $\hat{B} = e^{-\Delta\tau\hat{\mathcal{H}}}$ is the imaginary-time propagator over the discretization interval $\Delta\tau$.

Next, the Suzuki-Trotter (ST) approximation is applied to all imaginary-time slices l to factorize the various terms appearing in the exponentiated Hamiltonian [117, 118]. The resulting form for the partition function is

$$\mathcal{Z} \approx \text{Tr}[\hat{B}^{L_\tau}] + \mathcal{O}(\Delta\tau^2), \quad (15)$$

where the $\hat{B} \approx \hat{B} + \mathcal{O}(\Delta\tau^3)$ approximation

$$\hat{B} = e^{-\frac{\Delta\tau}{2}\hat{\mathcal{K}}} e^{-\Delta\tau\hat{\mathcal{V}}} e^{-\frac{\Delta\tau}{2}\hat{\mathcal{K}}} \quad (16)$$

is used. By applying cyclic property of the trace it is straightforward to see that Eq. (15) is left unchanged if the lower order $\hat{B} \approx \hat{B} + \mathcal{O}(\Delta\tau^2)$ approximation

$$\hat{B} = e^{-\Delta\tau\hat{\mathcal{V}}} e^{-\Delta\tau\hat{\mathcal{K}}} \quad (17)$$

is used instead. [SmoQyDQMC.jl](#) can run simulations based on applying either Eq. (16) or (17).

In cases where the kinetic energy operator $\hat{\mathcal{K}}$ is static, a formulation based on Eq. (17) is usually preferable as the computational overhead is lower. However, when e -ph interactions modulate the hopping amplitudes and the checkerboard approximation [119] is applied, it is better to use a formulation based on Eq. (16) as it improves the efficacy of this additional approximation; this aspect is discussed in greater detail in Sec. 3.5.

At this point, the only terms in the Hamiltonian that are not quadratic in Fermion creation and annihilation operators are $\hat{\mathcal{V}}_{\text{hub}}$ and $\hat{\mathcal{V}}_{\text{exh}}$. To handle these terms, the local and extended Hubbard interactions are decoupled using a HS transformation of the form

$$e^{-\Delta\tau U(\hat{n}_\uparrow - \frac{1}{2})(\hat{n}_\downarrow - \frac{1}{2})} = \sum_s e^{-S_{\text{hub}}(s) - \Delta\tau\hat{V}_{\text{hub}}(s)} \quad (18)$$

and

$$e^{-\Delta\tau V \sum_{\sigma,\sigma'} (\hat{n}_{\sigma,i} - \frac{1}{2})(\hat{n}_{\sigma',j} - \frac{1}{2})} = \sum_{s'} e^{-S_{\text{exh}}(s') - \Delta\tau\hat{V}_{\text{exh}}(s')}. \quad (19)$$

In Eq. (19) we have assumed that $i \neq j$ as the extended Hubbard interaction is between a distinct pair of electronic orbital states. Here, $\hat{V}_{\text{hub}}(s)$ and $\hat{V}_{\text{exh}}(s')$ are fermionic bilinear operators that depend on the HS fields s and s' , respectively, and the specific HS transformation used to decouple each interaction. Likewise, $S_{\text{hub}}(s)$ and $S_{\text{exh}}(s')$ are scalar functions of the HS fields that depend on which HS transformation was used. The different HS transformations that are available in [SmoQyDQMC.jl](#) are described in Appendix A.

Next, we evaluate the trace over the lattice degrees of freedom. This task is best accomplished in the position basis where we can analytically integrate out the phonon momentum operators $\hat{P}_{i,\nu}$. This allows the phonon position operators $\hat{X}_{i,\nu}$ to be replaced by the scalar phonon fields $x_{l,i}$ for all phonon modes $i = (i, \nu)$ and imaginary-time slices l [64, 69, 71, 75].

After these operations are performed, the resulting term that appears in the exponentiated Hamiltonian is a fermion operator that is bilinear in the electron annihilation and creation operators of the form

$$\hat{O}_{\sigma,l} = \hat{\mathbf{c}}_\sigma^\dagger O_{\sigma,l} \hat{\mathbf{c}}_\sigma, \quad (20)$$

where $\hat{\mathbf{c}}_\sigma^\dagger = [\hat{c}_{\sigma,1,1}^\dagger, \dots, \hat{c}_{\sigma,N,n}^\dagger]$ is a row-vector of creation operators for each of the \mathcal{N} orbitals in the system, and $\hat{\mathbf{c}}_\sigma$ is the corresponding column vector of annihilation operators. Therefore, $O_{\sigma,l}$ is a $\mathcal{N} \times \mathcal{N}$ Hermitian matrix.

The resulting expression for the partition function is

$$\mathcal{Z} \approx \sum_{s,s'} \int Dx e^{-S_B(s,s',x)} \prod_{\sigma=\uparrow,\downarrow} \text{Tr}_\sigma \left[\prod_{l=1}^{L_\tau} \hat{B}_{\sigma,l} \right], \quad (21)$$

with $\sum_{s,s'}$ and $\int \mathcal{D}x$ denoting the path integral over all HS fields $s_{l,i,\nu}$ and $s'_{l,i,\nu}$, and all phonon fields $x_{l,i,\nu}$, respectively. Here, $S_B(s,s',x)$ is the bosonic action and will be defined below in Eq. (30). The remaining trace Tr_σ runs over the spin- σ fermion degrees of freedom for a fixed HS and phonon field configuration (s,s',x) .

The propagator operators now explicitly depend on the spin σ and imaginary-time slice l and are given by

$$\hat{B}_{\sigma,l} = e^{-\frac{\Delta\tau}{2}\hat{\mathcal{K}}_{\sigma,l}} e^{-\Delta\tau\hat{\mathcal{V}}_{\sigma,l}} e^{-\frac{\Delta\tau}{2}\hat{\mathcal{K}}_{\sigma,l}}, \quad (22)$$

or

$$\hat{B}_{\sigma,l} = e^{-\Delta\tau\hat{\mathcal{V}}_{\sigma,l}} e^{-\Delta\tau\hat{\mathcal{K}}_{\sigma,l}}, \quad (23)$$

depending on whether the approximation from Eq. (16) or Eq. (17) is used, respectively. The dependence on the fields $s_{l,i,\nu}$ and $x_{l,i,\nu}$ appear as

$$\hat{\mathcal{K}}_{\sigma,l} = [\hat{\mathcal{K}}_{0,\sigma} + \hat{\mathcal{K}}_{\text{ssh},\sigma}(x_{l,i,\nu})] \quad (24)$$

in the electron kinetic energy, and

$$\hat{\mathcal{V}}_{\sigma,l} = [\hat{\mathcal{V}}_{0,\sigma} + \hat{\mathcal{V}}_{\text{hol},\sigma}(x_{l,i,\nu}) + \hat{\mathcal{V}}_{\text{hub},\sigma}(s_{l,i,\nu}) + \hat{\mathcal{V}}_{\text{exh},\sigma}(s'_{l,i,\nu})] \quad (25)$$

in the electron potential energy, respectively.

Employing the Blankenbecler, Scalapino and Sugar (BSS) relation [1], we integrate out the remaining Fermionic degrees of freedom to arrive at our final expression for the partition function

$$\mathcal{Z} \approx \sum_{s,s'} \int \mathcal{D}x e^{-S_B(s,s',x)} \prod_{\sigma=\uparrow,\downarrow} \det M_\sigma(\tau) + \mathcal{O}(\Delta\tau^2). \quad (26)$$

Here, $M_\sigma(\tau)$ is the spin- σ Fermion determinant matrix given by

$$M_\sigma(\tau) = I + B_{\sigma,l} B_{\sigma,l-1} \dots B_{\sigma,1} B_{\sigma,L_\tau} \dots B_{\sigma,l+1}, \quad (27)$$

where I is an $\mathcal{N} \times \mathcal{N}$ identity matrix and $B_{\sigma,l}$ are the spin- σ propagator matrices for imaginary-time slice l . Note that $\det M_\sigma(\tau)$ is the same for all values of τ . The propagator matrices take a similar form to the propagator operators appearing in Eq. (22) and Eq. (23), with

$$B_{\sigma,l} = e^{-\frac{\Delta\tau}{2}K_{\sigma,l}} e^{-\Delta\tau V_{\sigma,l}} e^{-\frac{\Delta\tau}{2}K_{\sigma,l}}, \quad (28)$$

or

$$B_{\sigma,l} = e^{-\Delta\tau V_{\sigma,l}} e^{-\Delta\tau K_{\sigma,l}}, \quad (29)$$

where $K_{\sigma,l}$ and $V_{\sigma,l}$ are the spin- σ electron kinetic and potential energy matrices for imaginary-time slice l , respectively. Each $K_{\sigma,l}$ is strictly off-diagonal and Hermitian, while the $V_{\sigma,l}$ matrices are diagonal.

In the most general case, the total bosonic action $S_B(x)$ appearing in Eq. (26) can be conveniently expressed as a sum of three terms

$$S_B(s,s'x) = S_{\text{hub}}(s) + S_{\text{exh}}(s') + S_{\text{ph}}(x). \quad (30)$$

The first two terms arise as a result of the HS transformations used to decouple the local and extended Hubbard interactions. Note that $S_{\text{hub}}(s)$ and $S_{\text{exh}}(s')$ may in general be complex. The third term $S_{\text{ph}}(x)$ is the total non-interacting phonon action, and is a strictly real valued function. The total phonon action itself can be conveniently expressed as the sum of four terms

$$S_{\text{ph}}(x) = S_{\text{qho}}(x) + S_{\text{anh}}(x) + S_{\text{disp}}(x) + S_{\text{hol}}(x). \quad (31)$$

The first term

$$S_{\text{qho}}(x) = \Delta\tau \sum_{\mathbf{i},\nu} \sum_l \left[\frac{M_{\mathbf{i},\nu} \Omega_{0,\mathbf{i},\nu}^2}{2} x_{l,\mathbf{i},\nu}^2 + \frac{M_{\mathbf{i},\nu}}{2} \left(\frac{x_{l+1,\mathbf{i},\nu} - x_{l,\mathbf{i},\nu}}{\Delta\tau} \right)^2 \right] \quad (32)$$

is the contribution to the bosonic action arising from the QHO term $\hat{\mathcal{U}}_{\text{qho}}$ in the Hamiltonian, as defined by Eq. (3). The term

$$S_{\text{anh}}(x) = \Delta\tau \sum_{\mathbf{i},\nu} \sum_l \frac{M_{\mathbf{i},\nu} \Omega_{a,\mathbf{i},\nu}^2}{24} x_{l,\mathbf{i},\nu}^4 \quad (33)$$

corresponds to the anharmonic lattice potential term $\hat{\mathcal{V}}_{\text{anh}}$ defined in Eq. (4). The third term

$$S_{\text{disp}}(x) = \Delta\tau \sum_{\mathbf{i},\nu} \sum_l \frac{M_{\mathbf{i},\nu} M_{\mathbf{j},\gamma}}{M_{\mathbf{i},\nu} + M_{\mathbf{j},\gamma}} \left[\tilde{\Omega}_{0,(\mathbf{i},\nu),(\mathbf{j},\gamma)}^2 (x_{l,\mathbf{i},\nu} - x_{l,\mathbf{j},\gamma})^2 + \frac{1}{12} \tilde{\Omega}_{a,(\mathbf{i},\nu),(\mathbf{j},\gamma)}^2 (x_{l,\mathbf{i},\nu} - x_{l,\mathbf{j},\gamma})^4 \right] \quad (34)$$

arises from dispersive couplings between QHO modes described by $\hat{\mathcal{U}}_{\text{disp}}$, defined in Eq. (5). The final term

$$S_{\text{hol}} = \begin{cases} -\frac{\Delta\tau}{2} \sum_{\sigma} \sum_{\mathbf{i},\nu} \sum_{\mathbf{j},\gamma} \left(\kappa_{\sigma,1,(\mathbf{i},\nu),(\mathbf{j},\gamma)} x_{l,\mathbf{i},\nu} + \kappa_{\sigma,3,(\mathbf{i},\nu),(\mathbf{j},\gamma)} x_{l,\mathbf{i},\nu}^3 \right) \\ 0 \end{cases} \quad (35)$$

arises due to the manner in which the Holstein-like interactions appearing in $\hat{\mathcal{V}}_{\text{hol}}$ are parameterized in Eq. (11).

The high-dimensional integral appearing in Eq. (26) is not analytically tractable but lends itself to a numerical solution. In particular, DQMC simulations perform a Monte Carlo sampling of the HS fields s and s' and phonon fields x , where the argument of the integral in Eq. (26) is the Monte Carlo weight

$$W(s, s', x) = e^{-S_B(s, s', x)} \prod_{\sigma=\uparrow,\downarrow} \det M_{\sigma}(\tau). \quad (36)$$

We note, however, that these Monte Carlo weights are not guaranteed to remain strictly positive. They can take on both positive and negative values in many cases, and can become complex if complex hopping amplitudes appear in the Hamiltonian or complex HS transformations are used to decouple the Hubbard interactions. This aspect leads to the well-known Fermion sign problem [120–122]. To circumvent this issue, DQMC instead takes the absolute value of Eq. (36) as the Monte Carlo weights

$$\overline{W}(s, s', x) = |W(s, s', x)| = e^{-\text{Re}\{S_B(s, s', x)\}} \prod_{\sigma=\uparrow,\downarrow} |\det M_{\sigma}(\tau)|. \quad (37)$$

Specifically, applying the Metropolis-Hastings criteria, the acceptance probability for updating the field configuration from (s_i, s'_i, x_i) to (s_f, s'_f, x_f) is given by

$$P_{(s_i, s'_i, x_i) \rightarrow (s_f, s'_f, x_f)} = \min \left(1, \frac{\overline{W}(s_f, s'_f, x_f)}{\overline{W}(s_i, s'_i, x_i)} \right). \quad (38)$$

However, using $\overline{W}(s, s', x)$ necessitates employing a reweighting procedure to recover unbiased measurements from a simulation; Sec. 3.10 discusses this procedure in more detail.

3.2 DQMC Simulation Overview

This section briefly outlines the overarching structure of a DQMC simulation. By design, this structure closely mirrors how scripts using `SmoQyDQMC.jl` are written to perform simulations. We have provided numerous examples of such scripts in the online [documentation](#), and Algorithm (1) provides an overview of what this structure might look like.

The goal of a DQMC simulation is to faithfully sample the relevant fields according to the probability distribution described by Eq. (37). In the case of `SmoQyDQMC.jl`, these fields correspond to either HS fields that result from decoupling the Hubbard interactions or the phonon fields. The fields are typically initialized to a random configuration at the beginning of a simulation. Then, updates to the field configurations are proposed using various methods, which are either accepted or rejected with a probability given by Eq. (38). Sec. 3.7 outlines an efficient procedure for updating the HS fields, whereas Secs. 3.8 and 3.9 describe methods for efficiently updating the phonon fields.

Another important part of the simulation is making measurements as field configurations are sampled. However, measurements should not be performed at the start of a simulation as the initial field configuration is typically far from the target equilibrium distribution described by Eq. (37). Therefore, the fields are first updated N_{therm} times during an initial thermalization period to equilibrate the field configurations to the target distribution. The remainder of the simulation is then broken into N_{bin} intervals, with n_{bin} updates performed per interval, as shown in Algorithm (1). After each set of updates to the field configurations, measurements are made and recorded. Electronic correlation measurements are made using the single-particle electron Green's function (which is defined and discussed in Sec. 3.3). At the end of each interval, the average of the previous n_{bin} measurements are written to the file. At the end of the simulation, these interval-averaged measurements are processed to generate final estimates for the expectation value of measured observables; the details of this analysis are discussed in Sec. 3.10. Algorithm (1) also shows how the chemical potential can be updated during a simulation to achieve a target electron density. Sec. 3.11 gives more details on this functionality.

Finally, the algorithms for updating fields and measuring electronic correlation functions require reliably calculating the single-particle electron Green's function matrices defined in Sec. 3.3. A naive approach to performing these calculations often results in numerical instabilities, rendering the result unreliable. Sec. 3.4 describes efficient algorithms for suppressing these numerical instabilities that would otherwise prevent the DQMC algorithm from functioning correctly.

3.3 Single-Particle Electron Green's Functions

A central quantity in DQMC simulations is the imaginary-time single-particle Green's function. This section provides a brief review of the definitions of this quantity and its properties.

The spin- σ electron Green's function in the orbital basis is given by

$$\mathcal{G}_{\sigma,\mathbf{i},\mathbf{j}}^{\nu,\gamma}(\tau, \tau') = \langle \hat{T} \hat{c}_{\sigma,\mathbf{i},\nu}(\tau) \hat{c}_{\sigma,\mathbf{j},\gamma}^\dagger(\tau') \rangle = \begin{cases} \langle \hat{c}_{\sigma,\mathbf{i},\nu}(\tau) \hat{c}_{\sigma,\mathbf{j},\gamma}^\dagger(\tau') \rangle & \text{if } \tau \geq \tau' \\ -\langle \hat{c}_{\sigma,\mathbf{j},\gamma}^\dagger(\tau') \hat{c}_{\sigma,\mathbf{i},\nu}(\tau) \rangle & \text{if } \tau < \tau', \end{cases} \quad (39)$$

where \hat{T} is the imaginary-time ordering operator. Eq. (39) describes the creation of a spin- σ electron at orbital γ in unit cell \mathbf{j} at imaginary-time τ' , and annihilation at orbital ν in unit cell \mathbf{i} at imaginary time τ . The imaginary-time axis spans the interval $0 \leq (\tau, \tau') < \beta$, and the electron Green's function is additionally subject to the aperiodic boundary condition

$$\mathcal{G}_{\sigma,\mathbf{i},\mathbf{j}}^{\nu,\gamma}(\tau - \beta, \tau') = -\mathcal{G}_{\sigma,\mathbf{i},\mathbf{j}}^{\nu,\gamma}(\tau, \tau') \quad (40)$$

Algorithm 1 Overview of DQMC simulation structure

```

Initialize Ising HS fields  $s$  and phonon fields  $x$  to random initial configuration.
for  $i \in [1, N_{\text{therm.}}]$  do
    Update Ising HS field  $s$  using algorithm from Sec. 3.7.
    Update phonon fields  $x$  using algorithms from Secs. 3.8 and 3.9.
    Update chemical potential; see Sec. 3.11.
end for
for bin  $\in [1, N_{\text{bins}}]$  do
    for  $i \in [1, n_{\text{bin}}]$  do
        Update Ising HS field  $s$  using algorithm from Sec. 3.7.
        Update phonon fields  $x$  using algorithms from Secs. 3.8 and 3.9.
        Make measurements; see Sec. 3.3.
        Update chemical potential; see Sec. 3.11.
    end for
    Write average value of measurements in current bin to file.
end for
Average binned measurements to get final estimates for measured observables; see Sec. 3.10.

```

when $\tau \neq \tau'$.

Given a fixed set of field configurations s , s' , and x , the equal-time Green's function can be related to the matrix elements of the Fermion determinant matrix by

$$G_\sigma(\tau, \tau) = M_\sigma^{-1}(\tau) = [I + B_\sigma(\tau, 0)B_\sigma(\beta, \tau)]^{-1}, \quad (41)$$

where we have used the short-hand notation

$$B_\sigma(\tau, \tau') = B_{\sigma, l}B_{\sigma, l-1} \dots B_{\sigma, 1}, \quad (42)$$

with $B_\sigma(\tau, \tau - \Delta\tau) = B_{\sigma, l}$ and $B_\sigma(\tau, \tau) = I$. Therefore,

$$G_\sigma(0, 0) = [I + B_\sigma(\beta, 0)]^{-1} = [I + B_{\sigma, L_\tau}B_{\sigma, L_\tau-1} \dots B_{\sigma, 1}]^{-1}, \quad (43)$$

subject to the boundary condition

$$G_\sigma(\beta, \beta) = G_\sigma(0, 0). \quad (44)$$

The equal-time Green's function matrix $G_\sigma(\tau, \tau)$ can be propagated to adjacent imaginary-time slices in the forward and reverse directions using the relations

$$G_\sigma(\tau + \Delta\tau, \tau + \Delta\tau) = B_{\sigma, l+1}G_\sigma(\tau, \tau)B_{\sigma, l+1}^{-1} \quad (45)$$

and

$$G_\sigma(\tau - \Delta\tau, \tau - \Delta\tau) = B_{\sigma, l}^{-1}G_\sigma(\tau, \tau)B_{\sigma, l}, \quad (46)$$

respectively. These relationships between the Green's functions on adjacent time-slices are the basis for an efficient updating scheme when performing Metropolis-Hastings or Heat-bath sampling [2], as discussed in Sec. 3.7.

The time-displaced (or unequal-time) Green's functions $\mathcal{G}_{\sigma, i, j}^{\nu, \gamma}(\tau, 0)$ and $\mathcal{G}_{\sigma, i, j}^{\nu, \gamma}(0, \tau)$ correspond to the matrix elements of

$$G_\sigma(\tau, 0) = B_\sigma(\tau, 0)G_\sigma(0, 0) \quad (47a)$$

$$= [B_\sigma^{-1}(\tau, 0) + B_\sigma(\beta, \tau)]^{-1} \quad (47b)$$

and

$$G_\sigma(0, \tau) = G_\sigma(0, 0^+) B_\sigma^{-1}(\tau, 0) \quad (48a)$$

$$= -[I - G_\sigma(0, 0)] B_\sigma^{-1}(\tau, 0) \quad (48a)$$

$$= -[B_\sigma^{-1}(\beta, \tau) + B_\sigma(\tau, 0)]^{-1}, \quad (48b)$$

respectively, where we have applied the boundary condition

$$G_\sigma(0, 0^+) = \lim_{\tau \rightarrow 0} G_\sigma(0, \tau) = -[I - G_\sigma(0, 0)]. \quad (49)$$

In similar fashion to the equal-time Green's function matrices, the time-displaced Green's function matrices can be propagated in the forward and reverse imaginary-time directions using the relations

$$G_\sigma(\tau, 0) = \begin{cases} B_\sigma(\tau, \tau') G_\sigma(\tau', 0) & \text{if } \beta > \tau > \tau' > 0 \\ B_\sigma^{-1}(\tau', \tau) G_\sigma(\tau', 0) & \text{if } \beta > \tau' > \tau > 0 \end{cases} \quad (50)$$

and

$$G_\sigma(0, \tau) = \begin{cases} G_\sigma(0, \tau') B_\sigma^{-1}(\tau, \tau') & \text{if } \beta > \tau > \tau' > 0 \\ G_\sigma(0, \tau') B_\sigma(\tau', \tau) & \text{if } \beta > \tau' > \tau > 0 \end{cases} \quad (51)$$

Specific boundary conditions arise as a result of the aperiodic boundary condition set by Eq. (40), and the definition of the Fermionic Green's function in Eq. (39). In particular, the time-displaced Green's function matrices satisfy

$$G_\sigma(\beta, 0) = \lim_{\tau \rightarrow \beta} G_\sigma(\tau, 0) = I - G_\sigma(0, 0) \quad (52)$$

$$G_\sigma(0, \beta) = \lim_{\tau \rightarrow \beta} G_\sigma(0, \tau) = -G_\sigma(0, 0), \quad (53)$$

where it is again assumed that $\tau > 0$.

Lastly, again assuming a fixed HS and phonon field configuration, higher order correlation functions can be measured by applying Wick's theorem to express them as sums of products of the single-particle electron Green's functions [19, 123].

3.4 Numerically Stable Framework for DQMC Simulations

The procedure for updating the HS ($s_{l,i,\nu}$) and phonon ($x_{l,n_{l,\nu}}$) fields requires calculating the equal-time Green's function matrices $G_\sigma(\tau, \tau)$ for all imaginary time slices $l \in [1, L_\tau]$. Similarly, performing measurements of any imaginary time-displaced correlation functions requires calculating the imaginary time-displaced Green's functions $G_\sigma(\tau, 0)$ and $G_\sigma(0, \tau)$.

A straightforward approach for computing these quantities is outlined in Algorithm 2. Unfortunately, this naive approach fails due to well-documented [2, 124–127] numerical instabilities associated with evaluating the ill-conditioned products of $B_{\sigma,l}$ matrices. Specifically, repeated matrix multiplication by the propagator matrices $B_{\sigma,l}$ accumulates numerical errors that quickly become severe. These numerical errors appear both when attempting to evaluate the $B_\sigma(\beta, 0)$ term appearing in Eq. (43), and also as a result of repeated applications of Eqs. (45), (50), and (51). The errors are then further amplified when matrix inversions are performed, as in Eq. (43).

Practical implementations of the DQMC algorithm have to overcome these numerical instabilities by introducing stable matrix factorizations [2, 124–127]. The `SmoQyDQMC.jl` package uses stabilization procedures based on those introduced in Ref. [125] and further discussed in Ref. [127]. Our package also stores intermediate matrix products to improve the algorithm's efficiency [5, 128, 129], an approach described in greater detail below. To outline this procedure, we first introduce the *LDR* matrix factorization, which represents products of propagator

matrices $B_{\sigma,l}$ and is based on the column-pivoted QR factorization. For a non-singular square matrix A , its column-pivoted QR factorization is given by

$$AP = QR', \quad (54)$$

where Q is a unitary matrix, R' is an upper-triangular matrix, and P is a permutation matrix. The corresponding $A = LDR$ factorization is then defined as product of matrices

$$L = Q, \quad (55a)$$

$$D = |\text{Diag}(R')|, \text{ and} \quad (55b)$$

$$R = |\text{Diag}(R')|^{-1} R' P^T. \quad (55c)$$

Here, both the unitary matrix L and matrix R are well-conditioned matrices, and D is a diagonal matrix. To further improve numerical stability, it is useful to factorize D as

$$D = D_{\max} D_{\min}, \quad (56)$$

where $D_{\max} = \max(D, 1)$ and $D_{\min} = \min(D, 1)$ [125].

Next, the imaginary-time axis of length L_τ is split into $N_s = L_\tau/n_s$ intervals of length n_s . The relative position within interval $n \in [1, N_s]$ is given by $l_n \in [1, n_s]$, where the corresponding imaginary-time slice is $l = l_n + (n-1)n_s$. For simplicity's sake, here we have assumed $\text{mod}(L_\tau, n_s) = 0$. While this will not be the case in general, it is relatively straightforward to generalize the algorithms outlined below to the case that this assumption does not hold.

The composite propagator matrix associated with an interval n is given by

$$\begin{aligned} \bar{B}_{\sigma,n} &= B_{\sigma,nn_s} B_{\sigma,nn_s-1} \dots B_{\sigma,(n-1)n_s+1} \\ &= B_\sigma(\Delta\tau n n_s, \Delta\tau (n-1) n_s), \end{aligned} \quad (57)$$

with the product of $\bar{B}_{\sigma,n}$ matrices represented by

$$\begin{aligned} \bar{B}_{\sigma,n,n'} &= \bar{B}_{\sigma,n} \bar{B}_{\sigma,n-1} \dots \bar{B}_{\sigma,n'+1} \\ &= B_{\sigma,nn_s} B_{\sigma,nn_s-1} \dots B_{\sigma,n'n_s+1} \\ &= B_\sigma(\Delta\tau n n_s, \Delta\tau n' n_s), \end{aligned} \quad (58)$$

where $n > n'$ and $\bar{B}_{\sigma,n,n-1} = \bar{B}_{\sigma,n}$. The corresponding LDR factorization for $\bar{B}_{\sigma,n,n'}$ is denoted by

$$\bar{F}_{\sigma,n,n'} = \bar{L}_{\sigma,n,n'} \bar{D}_{\sigma,n,n'} \bar{R}_{\sigma,n,n'}. \quad (59)$$

Algorithm 2 Numerically Unstable Forward Propagation Framework for DQMC Simulations

Calculate $G_\sigma(0,0)$ using Eq. (43): $G_\sigma(0,0) := [I + B_\sigma(\beta, 0)]^{-1}$.

Initialize $G_\sigma(\tau, \tau)$: $G_\sigma(\tau, \tau) := G_\sigma(0, 0)$.

Initialize $G_\sigma(\tau, 0)$: $G_\sigma(\tau, 0) := G_\sigma(0, 0)$.

Initialize $G_\sigma(0, \tau)$ by applying Eq. (49): $G_\sigma(0, \tau) := -[I - G_\sigma(0, 0)]$.

for $l \in 1, 2, \dots, L_\tau$ **do**

 Apply Eq. (45): $G_\sigma(\tau, \tau) := B_{\sigma,l} G_\sigma(\tau - \Delta\tau, \tau - \Delta\tau) B_{\sigma,l}^{-1}$.

 Apply Eq. (50): $G_\sigma(\tau, 0) := B_{\sigma,l} G_\sigma(\tau - \Delta\tau, 0)$.

 Apply Eq. (51): $G_\sigma(0, \tau) := G_\sigma(0, \tau - \Delta\tau) B_{\sigma,l}^{-1}$.

 [Insert Updates to Fields or Time-Displaced Correlation Measurements Here.]

end for

Algorithm 3a Numerically Stable Forward Propagation Framework for DQMC Simulations

Input: $G_\sigma(0, 0)$.

Input: $\bar{F}_\sigma = [\bar{F}_{\sigma, N_s, 0}, \bar{F}_{\sigma, N_s, 1}, \dots, \bar{F}_{\sigma, N_s, N_s-1}]$.

for $l \in 1, 2, \dots, L_\tau - 1, L_\tau$ **do**

 Calculate $l \rightarrow (n, l_n)$.

 Apply Eq. (45): $G_\sigma(\tau, \tau) := B_{\sigma, l} G_\sigma(\tau - \Delta\tau, \tau - \Delta\tau) B_{\sigma, l}^{-1}$.

 Apply Eq. (50): $G_\sigma(\tau, 0) := B_{\sigma, l} G_\sigma(\tau - \Delta\tau, 0)$.

 Apply Eq. (51): $G_\sigma(0, \tau) := G_\sigma(0, \tau - \Delta\tau) B_{\sigma, l}^{-1}$.

 [Insert Updates to Fields or Time-Displaced Correlation Measurements Here.]

if $l_n == n_s$ **then**

 Calculate $\bar{B}_{\sigma, n}$.

if $n == 1$ **then**

 Calculate $\bar{F}_{\sigma, 1, 0} := \bar{B}_{\sigma, 1}$.

else

 Retrieve $\bar{F}_{\sigma, n-1, 0} = \bar{F}_\sigma[n-1]$.

 Calculate $\bar{F}_{\sigma, n, 0} := \bar{B}_{\sigma, n} \bar{F}_{\sigma, n-1, 0}$ using stabilization routine B.1.

end if

 Set $\bar{F}_\sigma[n] := \bar{F}_{\sigma, n, 0}$.

if $l == L_\tau$ **then**

 Evaluate Eq. (43) using routine B.4: $G_\sigma(0, 0) := [1 + \bar{F}_{\sigma, N_s, 0}]^{-1}$.

 Evaluate Eq. (52): $G_\sigma(\beta, 0) := I - G_\sigma(0, 0)$.

 Evaluate Eq. (53): $G_\sigma(0, \beta) := -G_\sigma(0, 0)$.

else

 Retrieve $\bar{F}_{\sigma, N_s, n} = \bar{F}_\sigma[n+1]$.

 Evaluate Eq. (41) using routine B.3: $G_\sigma(\tau, \tau) := [I + \bar{F}_{\sigma, n, 0} \bar{F}_{\sigma, N_s, n}]^{-1}$.

 Evaluate Eq. (47b) using routine B.5: $G_\sigma(\tau, 0) := [\bar{F}_{\sigma, n, 0}^{-1} + \bar{F}_{\sigma, N_s, n}]^{-1}$.

 Evaluate Eq. (48b) using routine B.5: $G_\sigma(0, \tau) := -[\bar{F}_{\sigma, N_s, n}^{-1} + \bar{F}_{\sigma, n, 0}]^{-1}$.

end if

end if

end for

Output: $\bar{F}_\sigma = [\bar{F}_{\sigma, 1, 0}, \bar{F}_{\sigma, 2, 0}, \dots, \bar{F}_{\sigma, N_s, 0}]$.

Algorithm 3b Numerically Stable Reverse Propagation Framework for DQMC Simulations

Input: $G_\sigma(0, 0)$.

Input: $\bar{\mathbf{F}}_\sigma = [\bar{F}_{\sigma,1,0}, \bar{F}_{\sigma,2,0}, \dots, \bar{F}_{\sigma,N_s,0}]$.

for $l \in L_\tau, L_\tau - 1, \dots, 2, 1$ **do**

Calculate $l \rightarrow (n, l_n)$.

if $l == L_\tau$ **then**

Apply Eq. (52): $G_\sigma(\beta, 0) := I - G_\sigma(0, 0)$.

Apply Eq. (53): $G_\sigma(0, \beta) := -G_\sigma(0, 0)$.

else if $l_n \neq n_s$ **then**

Apply Eq. (46): $G_\sigma(\tau, \tau) := B_{\sigma, l+1}^{-1} G_\sigma(\tau + \Delta\tau, \tau + \Delta\tau) B_{\sigma, l+1}$.

Apply Eq. (50): $G_\sigma(\tau, 0) := B_{\sigma, l+1}^{-1} G_\sigma(\tau + \Delta\tau, 0)$.

Apply Eq. (51): $G_\sigma(0, \tau) := G_\sigma(0, \tau + \Delta\tau) B_{\sigma, l+1}$.

end if

[Insert Updates to Fields or Time-Displaced Correlation Measurements Here.]

if $l_n == 1$ **then**

Calculate $\bar{B}_{\sigma, n}$.

if $n == N_s$ **then**

Calculate $\bar{F}_{\sigma, N_s, N_s-1} := \bar{B}_{\sigma, n}$.

else

Retrieve $\bar{F}_{\sigma, N_s, n} = \bar{\mathbf{F}}_\sigma[n + 1]$.

Calculate $\bar{F}_{\sigma, N_s, n-1} := \bar{F}_{\sigma, N_s, n} \bar{B}_{\sigma, n}$ using stabilization routine B.2.

end if

Set $\bar{\mathbf{F}}_\sigma[n] := \bar{F}_{\sigma, N_s, n-1}$.

if $l == 1$ **then**

Evaluate Eq. (43): $G_\sigma(0, 0) := [1 + \bar{F}_{\sigma, N_s, 0}]^{-1}$.

Evaluate Eq. (52): $G_\sigma(\beta, 0) := I - G_\sigma(0, 0)$.

Evaluate Eq. (53): $G_\sigma(0, \beta) := -G_\sigma(0, 0)$.

else if $l_n == 1$ **then**

Retrieve $\bar{F}_{\sigma, n-1, 0} = \bar{\mathbf{F}}_\sigma[n - 1]$.

Evaluate Eq. (41) using routine B.4: $G_\sigma(\tau - \Delta\tau, \tau - \Delta\tau) := [I + \bar{F}_{\sigma, n-1, 0} \bar{F}_{\sigma, N_s, n-1}]^{-1}$.

Evaluate Eq. (47b) using routine B.5: $G_\sigma(\tau - \Delta\tau, 0) := [\bar{F}_{\sigma, n-1, 0}^{-1} + \bar{F}_{\sigma, N_s, n-1}]^{-1}$.

Evaluate Eq. (48b) using routine B.5: $G_\sigma(0, \tau - \Delta\tau) := -[\bar{F}_{\sigma, N_s, n-1}^{-1} + \bar{F}_{\sigma, n-1, 0}]^{-1}$.

end if

end if

end for

Output: $\bar{\mathbf{F}}_\sigma = [\bar{F}_{\sigma, N_s, 0}, \bar{F}_{\sigma, N_s, 1}, \dots, \bar{F}_{\sigma, N_s, N_s-1}]$.

Finally, $\bar{\mathbf{F}}_\sigma$ denotes an array of LDR factorizations of length N_s to store sequential $\bar{F}_{\sigma,n,n'}$ factorizations.

With these definitions in hand, we now turn our attention to Algorithms (3a) and (3b) for propagating the equal-time and time-displaced Green's function matrices in the forward ($\tau = 0 \rightarrow \tau = \beta$) and reverse ($\tau = \beta \rightarrow \tau = 0$) directions, respectively, in imaginary-time. In particular, note that the input state of that array $\bar{\mathbf{F}}$ in Algorithm (3b) matches the output state from Algorithm (3a). Likewise the input state of $\bar{\mathbf{F}}$ in Algorithm (3a) matches the output state from Algorithm (3b). Therefore, it is necessary to alternate the application of Algorithms (3a) and (3b). This results in a DQMC updating procedure that alternates sweeping forward and backward in imaginary time rather than cyclically. The advantage of this approach is that it allows the DQMC algorithm to retain a computational cost that scales linearly with β , while remaining numerically stable [128]. The parameter n_s is now understood to be the period in imaginary-time with which the Green's function matrices are re-computed using a more expensive, but numerically stable procedure.

In practice, it is important to monitor the numerical stability of a simulation to determine whether n_s needs to be decreased to increase numerical stability, or increased to reduce computational overhead. To accomplish this task, let $G_\sigma^{\text{stable}}(\tau, \tau)$ correspond to the equal-time Green's matrix that is recomputed using a numerically stable procedure, while $G_\sigma^{\text{naive}}(\tau, \tau)$ represents the same matrix, but generated via simple propagation in imaginary time using Eq. (45) or Eq. (46). We then keep track of the maximum element-wise difference

$$\delta G_\sigma = \max(|G_\sigma^{\text{stable}}(\tau, \tau) - G_\sigma^{\text{naive}}(\tau, \tau)|) \quad (60)$$

during a simulation. We would like δG_σ remain below some maximum threshold $\delta G_\sigma < \delta G_{\max}$, with $\delta G_{\max} \approx 10^{-6}$ a sufficient upper bound in most cases. Typical values for the period of numerical stabilization that satisfy this stability condition are $n_s \sim 5 - 10$, but depend on the strength of the interactions, inverse temperature β , and $\Delta\tau$. When this condition is being violated during a DQMC simulation, it is an indication that n_s may need to be reduced. Conversely, if $\delta G_\sigma \ll \delta G_{\max}$ throughout the simulation, then n_s can often be increased to reduce the simulation's run time. `SmoQyDQMC.jl` offers useful functionality for reducing n_s dynamically during a simulation if instances of $\delta G_\sigma > \delta G_{\max}$ are detected too frequently. However, it is worth noting that DQMC simulations performed with `SmoQyDQMC.jl` retain a computational cost that scales linearly with β for any n_s . Rather, reducing n_s simply increases the computational prefactor associated with the linear dependence on β .

3.5 The Checkerboard Approximation

The `SmoQyDQMC.jl` package makes heavy use of the checkerboard approximation [130]. For example, this approximation is necessary for efficiently simulating optical SSH e -ph interactions, where the hopping integrals are modulated by the atomic displacements of phonon modes defined to live on the sites of the lattice [116]. Note that `SmoQyDQMC.jl` does allow users to run simulations without the checkerboard approximation, but this will slow the code down significantly. The checkerboard approximation is also essential for computing exact HMC forces when simulating SSH models (see Sec. 3.8.1).

The checkerboard approximation is motivated by the observation that the exact exponentiated kinetic energy matrices

$$\Gamma_{\sigma,l}(\Delta\tau) = e^{-\Delta\tau K_{\sigma,l}} \quad (61)$$

appearing in the definition of the propagator matrices $B_{\sigma,l}$ are dense $\mathcal{N} \times \mathcal{N}$ matrices. As a result, evaluating the product of $B_{\sigma,l}$ with another dense matrix scales as $O(\mathcal{N}^3)$, and constitutes one of the leading computational costs in DQMC simulations. Moreover, when SSH-like e -ph interactions are present (arising from the \hat{K}_{ssh} term in the Hamiltonian), updating a phonon

field $x_{l,n_{i,v}}$ necessitates diagonalizing the corresponding spin- σ kinetic energy matrix $K_{\sigma,l}$ in order to re-exponentiate it. If this diagonalization is performed at every update, it would introduce an exorbitant additional computational cost and significantly slow the simulation. To ameliorate these computational hurdles, we introduce the order $O(\Delta\tau^2)$ checkerboard approximation, which replaces the $\Gamma_{\sigma,l}(\Delta\tau)$ dense matrices with sparse matrix representations. Applying this approximation reduces the cost of multiplying a dense matrix by $B_{\sigma,l}$ from $O(\mathcal{N}^3)$ to $O(\mathcal{N}^2)$. But more importantly, it reduces the cost of exponentiating the $K_{\sigma,l}$ matrices when a phonon field is updated from $O(\mathcal{N}^3)$ to $O(\mathcal{N})$.

Consider a spin- σ kinetic energy matrix $K_{\sigma,(i,j)} = -t_{\sigma,i,j}$, where $t_{\sigma,i,j}$ is the total hopping amplitude associated with the bond connecting orbitals i and j in the lattice. This matrix can be expressed as a sum of bond matrices $K_{\sigma} = \sum_b k_{\sigma,b}$. Here, b indexes each bond in the lattice, and the corresponding bond matrix is of the form

$$k_{\sigma,b} = \begin{bmatrix} \ddots & \vdots & & \vdots & \\ \dots & 0 & \dots & -t_{\sigma,i_b,j_b} & \dots \\ & \vdots & \ddots & \vdots & \\ \dots & -t_{\sigma,i_b,j_b}^* & \dots & 0 & \dots \\ & \vdots & \vdots & \ddots & \end{bmatrix}, \quad (62)$$

where a hopping amplitude may in general be complex, $t_{\sigma,i_b,j_b} = e^{i\phi_{\sigma,i_b,j_b}} |t_{\sigma,i_b,j_b}|$. For each bond matrix $k_{\sigma,b}$, a corresponding bond operator $\hat{k}_{\sigma,b} = -\sum_{\sigma} [t_{\sigma,i_b,j_b} \hat{c}_{\sigma,i_b}^{\dagger} \hat{c}_{\sigma,j_b} + \text{h.c.}]$ can be defined. Exponentiating $k_{\sigma,b}$ results in

$$e^{-\Delta\tau k_{\sigma,b}} = \begin{bmatrix} 1 & \vdots & & \vdots & \\ \dots & \cosh(\Delta\tau |t_{\sigma,i_b,j_b}|) & \dots & e^{i\phi_{\sigma,i_b,j_b}} \sinh(\Delta\tau |t_{\sigma,i_b,j_b}|) & \dots \\ & \vdots & 1 & \vdots & \\ \dots & e^{-i\phi_{\sigma,i_b,j_b}} \sinh(\Delta\tau |t_{\sigma,i_b,j_b}|) & \dots & \cosh(\Delta\tau |t_{\sigma,i_b,j_b}|) & \dots \\ & \vdots & & \vdots & 1 \end{bmatrix}. \quad (63)$$

Next, the bonds must be sorted into groups, or colors, such that the bonds of a given color do not overlap or touch. This condition corresponds to the bond operators \hat{k}_b (and corresponding matrices k_b) of the same color all mutually commuting with one another.

The task of constructing these groups can be reduced to the edge coloring problem in graph theory. It is important that the minimum number of colors is used, as this improves the accuracy of the checkerboard approximation. However, the precise composition of each color is not unique, and some coloring schemes are better than others. In this code, the colors are assigned by systematically iterating over the unit cells in the lattice, and assigning a color to each bond with a site contained in the current unit cell; for more information, we refer the reader to our [Checkerboard.jl](#) package [131].

Having assigned a color to each bond in the lattice, the total kinetic energy matrix may be expressed as

$$K_{\sigma} = \sum_{c=1}^{N_c} K_{\sigma,c} = \sum_{c=1}^{N_c} \left[\sum_{b \in c} k_{\sigma,b} \right], \quad (64)$$

where $K_{\sigma,c}$ is the kinetic energy matrix associated with just the bonds b assigned the color c , with N_c the number of colors. Absent any approximation, the exponential of a single color matrix $K_{\sigma,c}$ is given by

$$\Gamma_{\sigma,c}(\Delta\tau) = e^{-\Delta\tau K_{\sigma,c}} = \prod_{b \in c} e^{-\Delta\tau k_{\sigma,b}}. \quad (65)$$

With these definitions in hand, the checkerboard approximation is given by

$$\Gamma_\sigma(\Delta\tau) \approx \tilde{\Gamma}_\sigma(\Delta\tau) + O(\Delta\tau^2), \quad (66)$$

where

$$\tilde{\Gamma}_\sigma(\Delta\tau) = \Gamma_{\sigma,N_c}(\Delta\tau) \dots \Gamma_{\sigma,c}(\Delta\tau) \dots \Gamma_{\sigma,1}(\Delta\tau) \quad (67)$$

is the checkerboard matrix. A simple and efficient method for multiplying a dense matrix by $\tilde{\Gamma}_\sigma(\Delta\tau)$ is given by Algorithm 2 in Ref. [130].

The efficacy of the checkerboard approximation deteriorates in models with longer range hopping. This occurs due to the increase in the average coordination number with distance, increasing the number of color groups needed to partition the bonds. Moreover, while $\Gamma_\sigma(\Delta\tau)$ is Hermitian, the checkerboard matrix $\tilde{\Gamma}_\sigma(\Delta\tau)$ is not. In order to mitigate concerns regarding the accuracy of the checkerboard approximation, a symmetrized form $\tilde{\Gamma}_\sigma^\dagger(\frac{\Delta\tau}{2}) \cdot \tilde{\Gamma}_\sigma(\frac{\Delta\tau}{2})$ can be used instead. This form results in a Hermitian checkerboard matrix and significantly improves the overall accuracy of the checkerboard approximation [132]. In a DQMC simulation, this corresponds to using the checkerboard approximation in conjunction with the symmetric definition for the propagator matrices $B_{\sigma,l}$, as defined by Eq. (28).

`SmoQyDQMC.jl` has support for both the asymmetric or symmetric checkerboard approximation. When performing simulations models that include SSH interactions, it is recommended that the symmetric checkerboard approximation be used in order to help ensure the efficacy of the approximation.

3.6 Twisted Boundary Conditions

Version 2.0 of `SmoQyDQMC.jl` provides convenient integrated support for twisted boundary conditions (TBC) [133–137]. For a finite-size periodic lattice, the momentum grid is given by

$$\mathbf{k} = \sum_{d=1}^D \frac{n_d}{L_d} \mathbf{b}_d \quad (68)$$

for all integers $n_d \in [0, L_d]$, where D is the dimensionality of the lattice, \mathbf{a}_d are the lattice vectors, \mathbf{b}_d are the corresponding reciprocal lattice vectors, and L_d is the extent of the lattice in unit cells in the \mathbf{a}_d direction. Next, consider the hopping amplitude $t_{\sigma,(i,\nu),(j,\gamma)}$ in Eq. (7), which connects orbital γ in unit cell j to orbital ν in unit cell i . Applying TBC corresponds to the transformation

$$\tilde{t}_{\sigma,(i,\nu),(j,\gamma)} = e^{-i\theta_\sigma \cdot \mathbf{r}_{(i,\nu),(j,\gamma)}} t_{\sigma,(i,\nu),(j,\gamma)}, \quad (69)$$

where $\mathbf{r}_{(i,\nu),(j,\gamma)} = (\mathbf{i} + \mathbf{r}_\nu) - (\mathbf{j} + \mathbf{r}_\gamma)$ is the displacement vector separating the pair of orbitals, and θ_σ is the applied twist. This transformation effectively shifts the spin- σ electron momentum grid to

$$\tilde{\mathbf{k}}_\sigma = \mathbf{k} + \theta_\sigma \quad (70)$$

where the twist is parameterized as

$$\theta_\sigma = \sum_{d=1}^D \frac{\eta_{\sigma,d}}{L_d} \mathbf{b}_d. \quad (71)$$

The parameters $\eta_{\sigma,d} \in [0, 1]$ control the twist angle, with $\eta_{\sigma,d} = 0.0$ (0.5) corresponding to periodic (aperiodic) boundary conditions. Note that this transformation is also applied to the SSH-like e - ph coupling term in the Hamiltonian such that the coupling constant is transformed as

$$\tilde{\alpha}_{\sigma,m,(i,\nu,\eta),(j,\gamma,\rho)} = e^{-i\theta_\sigma \cdot \mathbf{r}_{(i,\nu),(j,\gamma)}} \alpha_{\sigma,m,(i,\nu,\eta),(j,\gamma,\rho)} \quad (72)$$

in Eq. (8).

3.7 Efficient Local Updates of Hubbard-Stratonovich Fields

In this section, we outline a well-known method for efficiently updating HS fields like those introduced in Sec. 3.1 to decouple Hubbard interactions [2]. We will describe this method within the context of the discrete spin-channel HS transformation introduced in Ref. [138] and defined in Appendix A.1.1. Note, though, that this same approach may be adapted to the other types of HS transformations used to decouple the local and extended Hubbard interactions [139, 140]. For a more general discussion on how to define and update HS transformations for other types of fermionic interactions, we refer readers to Refs. [19] and [123].

A naive, or brute-force, approach to updating the HS fields consists of re-calculating the fermion determinants from scratch each time an update to a field $s_{l,i,\nu}$ is proposed. Updating a single field would then scale as $O(\mathcal{N}^3)$, with the resulting computational cost to update all HS fields in space and imaginary time scaling as $O(\beta\mathcal{N}^4)$. It is possible, however, to reduce the cost of updating a single HS field from $O(\mathcal{N}^3)$ to $O(\mathcal{N}^2)$ by taking advantage of the fact that the $e^{-\Delta\tau V_{\sigma,l}}$ matrices that appear in the definition of the propagator matrices are diagonal [2]. This property allows one to reduce the computational complexity of updating all HS fields from $O(\beta\mathcal{N}^4)$ to $O(\beta\mathcal{N}^3)$.

We will assume an asymmetric form for the $B_{\sigma,l}$ matrices in the following discussion, as defined in Eq. (29). Given an update to a single HS field ($s_{l,i,\nu} \rightarrow s'_{l,i,\nu}$), the corresponding change in the propagator matrix may be expressed as

$$B'_{\sigma,l} = [I + \Delta_{\sigma}(\tau, i)]B_{\sigma,l}, \quad (73)$$

where

$$\Delta_{\sigma}(\tau, i) = \begin{bmatrix} 0 & & & & \\ & \ddots & & & \\ & & e^{\sigma\alpha(s'_{l,i} - s_{l,i})} - 1 & & \\ & & & \ddots & \\ & & & & 0 \end{bmatrix} \quad (74)$$

is a matrix with a single non-zero matrix element at index i on the diagonal. Employing the Sherman-Morrison matrix identity, one can show that the change in the corresponding fermion matrix determinant is given by the scalar equation

$$\begin{aligned} R_{\sigma}(s_{l,i,\nu} \rightarrow s'_{l,i,\nu}) &= \frac{\det G_{\sigma}(\tau, \tau)}{\det G'_{\sigma}(\tau, \tau)} \\ &= \det [I + \Delta_{\sigma}(\tau, i)(I - G_{\sigma}(\tau, \tau))] \\ &= 1 + \Delta_{\sigma,i,i}(\tau, i)(1 - G_{\sigma,i,i}(\tau, \tau)). \end{aligned} \quad (75)$$

The updated Green's function matrix can then be efficiently calculated from the old one using the rank-1 update

$$G'_{\sigma}(\tau, \tau) = G_{\sigma}(\tau, \tau) [I - R_{\sigma}^{-1} \Delta_{\sigma}(\tau, i)(I - G_{\sigma}(\tau, \tau))], \quad (76)$$

which in terms of matrix elements is

$$G'_{\sigma,j,k}(\tau, \tau) = G_{\sigma,j,k}(\tau, \tau) - R_{\sigma}^{-1} G_{\sigma,j,i}(\tau, \tau) \Delta_{\sigma,i,i}(\tau, i) [\delta_{i,k} - G_{\sigma,i,k}(\tau, \tau)]. \quad (77)$$

Additional gains in efficiency can also be made by accumulating these updates in a delayed updating scheme [141].

This local updating scheme forms the basis for efficiently sampling HS fields across all spatial sites and imaginary times. One begins by proposing and accepting/rejecting updates

to the HS fields for a single time slice, requiring $O(\mathcal{N}^3)$ operations. After all of the updates have been proposed for this imaginary time, the Green's function is advanced to the next time slice using Eq. (45), and the process is repeated. In practice, the imaginary time axis is sequentially iterated over, and Eq. (75) and Eq. (77) are used to efficiently update the HS fields at each imaginary time slice. While algorithms (3a) and (3b) are used to iterate over the imaginary time slices, the order the HS fields are iterated over at each time-slice is randomized to help reduce autocorrelation times. Note that a similar approach may be used to sample the fields when the symmetric definition for the $B_{\sigma,l}$ matrices [Eq. (28)] is used. However, in this case the Green's function matrix appearing in eqs. (75) to (77) is replaced by

$$\tilde{G}_\sigma(\tau, \tau) = e^{\frac{\Delta\tau}{2} K_l} G_\sigma(\tau, \tau) e^{-\frac{\Delta\tau}{2} K_l}. \quad (78)$$

Finally, we note that the same updating scheme can be used to sample the phonon fields in certain types of electron-phonon models (e.g. the Holstein model). However, it is not straightforward, or even necessarily possible, to formulate an efficient local updating scheme for arbitrary types of electron-phonon interactions. Moreover, even when local updates can be used they are inefficient at de-correlating the phonon fields, particularly when the phonon energy is much smaller than the electronic hopping ($\Omega/t \lesssim 0.5$) [75, 142, 143]. Various alternative sampling methods have been proposed, including self-learning Monte Carlo [142, 143] and Langevin and HMC methods [100, 102, 144, 145], which can reduce the autocorrelation time associated with sampling the phonon fields. `SmoQyDQMC.jl` uses an optimized HMC method for sampling the phonon fields, as outlined in the next section.

3.8 HMC Updates of Phonon Fields

In the `SmoQyDQMC.jl` package, specialized hybrid Monte Carlo (HMC) updates are used to sample the phonon fields in DQMC simulations of *e*-*ph* models. The HMC method, also frequently referred to as Hamiltonian Monte Carlo, was first developed by the lattice gauge theory community [100], and has since become a widely used tool for sampling continuous random variables more broadly [145]. In an HMC update, the phonon fields evolve according to a fictitious Hamiltonian dynamics to construct proposed global updates to every phonon field simultaneously.

To define the fictitious Hamiltonian dynamics, the DQMC Monte Carlo weight defined in Eq. (37) is re-expressed as

$$\overline{W}(s, s', x) = e^{-S(s, s', x)}, \quad (79)$$

where

$$S(s, s', x) = S_B(s, s', x) + S_F(s, s', x) \quad (80)$$

defines an effective action. The first term $S_B(s, s', x)$, given by Eq. (30), is the purely bosonic contribution to the total action. The second term $S_F(s, s', x)$ describes the fermionic contribution, and is given by

$$S_F(s, s', x) = \sum_\sigma S_{F,\sigma}(s, s', x) = \sum_\sigma \log |\det G_\sigma(\tau, \tau)|, \quad (81)$$

valid for all τ . Moving forward, we shall suppress reference to the HS fields s and s' , as they will be treated as a constant while updating the phonon fields x .

Next, a conjugate momentum p is introduced for each phonon field x , allowing us to define an effective Hamiltonian

$$H(x, p) = S(x) + \frac{1}{2} p^T \mathcal{M}^{-1} p, \quad (82)$$

which may be interpreted as the sum of “potential” and “kinetic” energies, where \mathcal{M} is a positive-definite dynamical mass matrix. The corresponding Hamiltonian equations of motion are

$$\begin{aligned}\dot{p} &= -\frac{\partial H}{\partial x} = -\frac{\partial S}{\partial x} \\ \dot{x} &= \frac{\partial H}{\partial p} = \mathcal{M}^{-1}p,\end{aligned}\tag{83}$$

defining a symplectic, time-reversible, and energy-conserving dynamics.

The first step in performing an HMC update is to directly sample the momentum according to the equilibrium Boltzmann distribution $\exp(-p^T \mathcal{M}^{-1} p / 2)$ according to

$$p = \sqrt{\mathcal{M}}R,\tag{84}$$

where each element of the random vector R is drawn from a standard normal distribution. In the simplest approach, the dynamical mass matrix is set to the identity, $\mathcal{M} = I$. Next, the Hamiltonian dynamics are evolved for N_t time-steps using the leapfrog integration method

$$\begin{aligned}p_{t+1/2} &= p_t + \frac{\Delta t}{2} f_t \\ x_{t+1} &= x_t + \Delta t \mathcal{M}^{-1} p_{t+1/2} \\ p_{t+1} &= p_{t+1/2} + \frac{\Delta t}{2} f_{t+1},\end{aligned}\tag{85}$$

where Δt is the integration step size and

$$f_t = -\frac{\partial S}{\partial x_t}\tag{86}$$

is the force driving the dynamics. Like the underlying Hamiltonian dynamics, the leapfrog integration method is symplectic and time-reversible. As a result, absent numerical instabilities, the total energy $H(x)$ will be conserved to $O(\Delta t^2)$ for arbitrarily long trajectories. Lastly, the final state (x_f, p_f) of the HMC trajectory replaces the initial state (x_i, p_i) with a probability given by the Metropolis-Hastings criteria

$$P = \min(1, e^{-\Delta H}),\tag{87}$$

where $\Delta H = H(x_f, p_f) - H(x_i, p_i)$. Crucially, the HMC method exactly satisfies detailed balance as a result of the leapfrog integration method being time-reversible and symplectic.

The most expensive part of performing an HMC update is evaluating the derivative of the action

$$\frac{\partial S}{\partial x} = \frac{\partial S_B}{\partial x} + \frac{\partial S_F}{\partial x}.\tag{88}$$

More specifically, evaluating the fermionic contribution to the derivative $\frac{\partial S_F}{\partial x}$ is the dominant cost, scaling as $O(\beta \mathcal{N}^3)$; Sec. 3.8.1 discusses how to evaluate this derivative.

Unfortunately, applying the basic HMC method outlined in this section still results in long autocorrelation times that stem from the disparate timescales introduced to the Hamiltonian dynamics by the bosonic action $S_B(x)$. Sec. 3.8.2 introduces a refined HMC method that utilizes two complementary methods for addressing this issue. Sec. 3.9 discusses intermittently supplementing the HMC updates with other types of global updates to help further reduce autocorrelation times and mitigate ergodicity concerns in certain situations. Lastly, while one might consider decoupling the Hubbard interaction using continuous HS fields which could then be sampled with HMC updates, the absence of a bosonic contribution coupling those fields in the imaginary time direction is known to make the approach challenging in practice [99, 101].

3.8.1 Evaluating the Derivative of the Action

The most computationally expensive aspect of performing a HMC update is calculating the derivative of the action at each time step during the HMC trajectory. The derivative of the bosonic action $S_B(x)$ is straightforward and fast to evaluate, with a computational cost that scales as $O(\beta\mathcal{N})$.

Taking the derivative of the fermionic action for a single spin species $S_F(x)$ is both more involved, and more computationally expensive, scaling as $O(\beta\mathcal{N}^3)$. The derivative of the fermionic action for just a single spin species $S_{F,\sigma}(x)$, as defined in Eq. (81), is

$$\frac{\partial S_{F,\sigma}}{\partial x_{l,n}} = \text{Re} \left\{ \text{Tr} \left[\frac{\partial B_{\sigma,l}}{\partial x_{l,n}} B_{\sigma,l}^{-1} (G_{\sigma}(\tau, \tau) - I) \right] \right\}, \quad (89)$$

where l is the imaginary time slice and n specifies the phonon mode.

In the case that the propagator matrices $B_{\sigma,l}$ are defined using the asymmetric definition given in Eq. (29), then Eq. (89) becomes

$$\frac{\partial S_{F,\sigma}}{\partial x_{l,n}} = \text{Re} \left\{ \text{Tr} \left[\frac{\partial \Lambda_{\sigma,l}}{\partial x_{l,n}} \Lambda_{\sigma,l}^{-1} (G_{\sigma}(\tau, \tau) - I) \right] \right\} + \text{Re} \left\{ \text{Tr} \left[\frac{\partial \Gamma_{\sigma,l}}{\partial x_{l,n}} \Gamma_{\sigma,l}^{-1} (\Lambda_l^{-1} G_{\sigma}(\tau, \tau) \Lambda_l - I) \right] \right\}, \quad (90)$$

where $\Lambda_{\sigma,l} = \exp(-\Delta\tau V_{\sigma,l})$ and $\Gamma_{\sigma,l} = \exp(-\Delta\tau K_{\sigma,l})$. If the $B_{\sigma,l}$ matrices are instead defined using the symmetric definition given in (28), then Eq. (89) instead becomes

$$\begin{aligned} \frac{\partial S_{F,\sigma}}{\partial x_{l,n}} = & \text{Re} \left\{ \text{Tr} \left[\frac{\partial \Gamma_{\sigma,l}}{\partial x_{l,n}} \Gamma_{\sigma,l}^{-1} (G_{\sigma}(\tau, \tau) - I) \right] \right\} + \text{Re} \left\{ \text{Tr} \left[\frac{\partial \Lambda_{\sigma,l}}{\partial x_{l,n}} \Lambda_{\sigma,l}^{-1} (\Gamma_{\sigma,l}^{-1} G_{\sigma}(\tau, \tau) \Gamma_{\sigma,l} - I) \right] \right\} \\ & + \text{Re} \left\{ \text{Tr} \left[\frac{\partial \Gamma_{\sigma,l}^{\dagger}}{\partial x_{l,n}} \Gamma_{\sigma,l}^{-\dagger} (\Lambda_{\sigma,l}^{-1} \Gamma_{\sigma,l}^{-1} G_{\sigma}(\tau, \tau) \Gamma_{\sigma,l} \Lambda_{\sigma,l} - I) \right] \right\}, \end{aligned} \quad (91)$$

where $\Lambda_{\sigma,l} = \exp(-\Delta\tau V_{\sigma,l})$ and $\Gamma_{\sigma,l} = \exp(-\Delta\tau K_l/2)$.

At this point, the diagonal structure of the exponentiated potential energy matrix $\Lambda_{\sigma,l}$ allows for the simplification

$$\text{Tr} \left[\frac{\partial \Lambda_{\sigma,l}}{\partial x_{l,n}} \Lambda_{\sigma,l}^{-1} A \right] = -\Delta\tau \text{Tr} \left[\frac{\partial V_{\sigma,l}}{\partial x_{l,n}} A \right] \quad (92)$$

to be applied to equations (90) and (91), where A is an $\mathcal{N} \times \mathcal{N}$ matrix. In the case of the exact exponentiated kinetic energy matrix $\Gamma_{\sigma,l}$, on the other hand, only an approximate simplification

$$\text{Tr} \left[\frac{\partial \Gamma_{\sigma,l}}{\partial x_{l,n}} \Gamma_{\sigma,l}^{-1} A \right] \approx -\Delta\tau \text{Tr} \left[\frac{\partial K_{\sigma,l}}{\partial x_{l,n}} A \right] + \mathcal{O}(\Delta\tau^2) \quad (93)$$

can be made. However, if the checkerboard approximation is used, then repeated application of the chain rule and cyclic property of the trace results in the exact expression

$$\text{Tr} \left[\frac{\partial \tilde{\Gamma}_{\sigma,l}}{\partial x_{l,n}} \tilde{\Gamma}_{\sigma,l}^{-1} A \right] = -\Delta\tau \sum_{c=1}^{N_c} \left(\text{Tr} \left[\frac{\partial K_{\sigma,l,c}}{\partial x_{l,n}} (\Gamma_{\sigma,l,c+1}^{-1} \dots \Gamma_{\sigma,l,N_c}^{-1} A \Gamma_{\sigma,l,N_c} \dots \Gamma_{\sigma,l,c+1}) \right] \right), \quad (94)$$

where $\tilde{\Gamma}_{\sigma,l}$ is the checkerboard approximation matrix for $\Gamma_{\sigma,l}$ as defined in Eq. (67). The above equation holds because $\left[\frac{\partial K_{\sigma,l,c}}{\partial x_{l,n}}, K_{\sigma,l,c} \right] = 0$ for any color matrix $K_{\sigma,l,c}$ as defined in Eq. (64). Similarly, the simplification

$$\text{Tr} \left[\frac{\partial \tilde{\Gamma}_{\sigma,l}^{\dagger}}{\partial x_{l,n}} \tilde{\Gamma}_{\sigma,l}^{-\dagger} A \right] = -\Delta\tau \sum_{c=1}^{N_c} \left(\text{Tr} \left[\frac{\partial K_{\sigma,l,c}}{\partial x_{l,n}} (\Gamma_{\sigma,l,c-1}^{-1} \dots \Gamma_{\sigma,l,1}^{-1} A \Gamma_{\sigma,l,1} \dots \Gamma_{\sigma,l,c-1}) \right] \right) \quad (95)$$

can be made as well.

In practice, to evaluate the derivative of the action, we sequentially iterate over the imaginary time axis using Algorithm (3a) or (3b), generating each equal-time Green's function matrix $G_\sigma(\tau, \tau)$. This matrix is then used to calculate the derivative of the action with respect to the phonon fields for the current imaginary time slice. Doing this for each imaginary time slice, we evaluate the derivative of the action with respect to all the phonon fields while retaining $O(\beta \mathcal{N}^3)$ scaling in the DQMC simulations.

3.8.2 Resolving Disparate Timescales in the Bosonic Action

In this section, we consider an isolated QHO with mass M ; generalizing this discussion to a collection of QHOs is straightforward.

An important cause of long autocorrelation times in DQMC simulations of e -ph models is the QHO action $S_{\text{qho}}(x)$, defined in Eq. (32). The action associated with a single QHO is

$$S_{\text{qho}}(x) = \Delta\tau \sum_l \left[\frac{M\Omega^2}{2} x_l^2 + \frac{M}{2} \left(\frac{x_{l+1} - x_l}{\Delta\tau} \right)^2 \right], \quad (96)$$

with the resulting the resulting forces in a corresponding Hamiltonian dynamics given by

$$f_{\text{qho},l} = -\frac{\partial S_{\text{qho}}}{\partial x_l} = -\Delta\tau M \left[\Omega^2 x_l + (2x_l - x_{l+1} - x_{l-1})/\Delta\tau^2 \right]. \quad (97)$$

Next, defining the discrete Fourier transform in imaginary time as

$$\tilde{f}_n = \mathcal{F} \cdot f_l = \frac{1}{\sqrt{L_\tau}} \sum_l e^{-i\frac{2\pi}{L_\tau} nl} f_l \quad (98)$$

and applying it to $f_{\text{qho},l}$ results in

$$\tilde{f}_{\text{qho},n} = -\Delta\tau M \Omega^2 \left[1 + \frac{4}{\Delta\tau^2 \Omega^2} \sin^2 \left(\frac{\pi n}{L_\tau} \right) \right] \tilde{x}_n, \quad (99)$$

for $n \in [0, L_\tau)$ and $\tau = l \cdot \Delta\tau$. The dynamical modes \tilde{x}_n are the Fourier transform of the phonon fields in imaginary time x_l .

The resulting Hamiltonian equations of motion in frequency space associated with $S_{\text{qho}}(x)$ are given by

$$\begin{aligned} \dot{\tilde{p}}_n &= -\tilde{k}_n \tilde{x}_n \\ \dot{\tilde{x}}_n &= \tilde{M}_n^{-1} \tilde{p}_n, \end{aligned} \quad (100)$$

which describes a system of L_τ independent harmonic oscillators with spring constants

$$\tilde{k}_n = \Delta\tau M \Omega^2 \left[1 + \frac{4}{\Delta\tau^2 \Omega^2} \sin^2 \left(\frac{\pi n}{L_\tau} \right) \right]. \quad (101)$$

The resulting ratio of the magnitude of the forces for the fastest ($\tilde{x}_{L_\tau/2}$) and slowest (\tilde{x}_0) dynamical modes is

$$\frac{\tilde{k}_{L_\tau/2}}{\tilde{k}_0} = \left[1 + \frac{4}{\Delta\tau^2 \Omega^2} \right] \gg 1, \quad (102)$$

demonstrating that $S_{\text{qho}}(x)$ introduces disparate timescales to the dynamics, especially as one must choose $\Delta\tau$ small to preserve the accuracy of the Trotter approximation.

This situation results in standard HMC updates needing to use a small integration time-step Δt to resolve the high frequency dynamical modes, resulting in long autocorrelation times for

the low frequency dynamical modes. Similarly, when performing local updates, the proposed change to a phonon field needs to be small relative to the QHO characteristic length scale $\Delta X = 1/\sqrt{2M\Omega}$ to attain a reasonable acceptance rate. Reducing the size of these changes will again give rise to long autocorrelation times.

One successful approach for addressing this issue is the Fourier acceleration method, whereby carefully selected values for the dynamical mass \tilde{M}_n appearing in Eq. (100) are selected so as to reduce autocorrelation times [67, 102, 144, 146, 147]. Specifically, the dynamically masses are given by

$$\tilde{M}_n = \Delta\tau M\Omega^2 \left[1 + \frac{4}{\Delta\tau^2\Omega_{\text{reg}}^2} \sin^2\left(\frac{\pi n}{L_\tau}\right) \right], \quad (103)$$

where $\Omega_{\text{reg}} = \sqrt{1 + \eta_{\text{reg}}^2}\Omega$ and $\eta_{\text{reg}} \in \mathbb{R}_{\geq 0}$ acts as a regularization parameter. Transforming back to imaginary time, this corresponds to a dynamical mass matrix, as appears in Eq. (83), given by

$$\mathcal{M} = \mathcal{F}^\dagger \tilde{M} \mathcal{F}, \quad (104)$$

where \tilde{M} is a diagonal matrix with the values along the diagonal given by Eq. (103). In the case that $\eta_{\text{reg}} = 0$, the dynamical frequencies $\tilde{\omega}_n = \sqrt{\tilde{k}_n/\tilde{M}_n}$ for the harmonic oscillators described by Eq. (100) all get normalized to unity, resulting in all the dynamical modes \tilde{x}_n evolving at the same rate. In the opposite limit that $\eta_{\text{reg}} = \infty$, the dynamical mass matrix simply reduces to the scalar value $\mathcal{M} = \Delta\tau M\Omega^2$. Intuitively, decreasing η_{reg} from infinity to zero should be thought of as increasing the mass of the high-frequency dynamical modes, thereby slowing them down so that they evolve at the same rate as the low-frequency dynamical modes.

[SmoQyDQMC.jl](#) uses a modified version of the exact Fourier acceleration hybrid Monte Carlo (EFA-HMC) method that first introduced in Ref. [148] and then improved upon in Ref. [103]. This approach takes advantage of the fact that the equations of motion in Eq. (100) are analytically integrable using the solution

$$\begin{aligned} \tilde{x}_n(t) &= \tilde{x}_n(0) \cos(\tilde{\omega}_n t) + \tilde{p}_n(0) \sin(\tilde{\omega}_n t) / (\tilde{M}_n \tilde{\omega}_n) \\ \tilde{p}_n(t) &= \tilde{p}_n(0) \cos(\tilde{\omega}_n t) - \tilde{x}_n(0) \sin(\tilde{\omega}_n t) \times (\tilde{M}_n \tilde{\omega}_n), \end{aligned} \quad (105)$$

given the initial conditions $\tilde{x}_n(0)$ and $\tilde{p}_n(0)$ for each dynamical mode. This analytic integration of the phonon fields and conjugate momentum, referred to as exact Fourier acceleration (EFA), is outlined in Algorithm (4). The full EFA-HMC method used in [SmoQyDQMC.jl](#) is then presented in Algorithm (5). An important detail in Algorithm (5) is that the time-step is randomized at the start of each HMC trajectory, with the amount of randomization controlled by the parameter $\delta \in (-1, 1)$. This practice helps avoid ergodicity concerns that can arise as the result of quasi-periodic behavior, an issue that can occur when the electrons only weakly couple to the high frequency modes in the dynamics [149].

It should be noted that when $\eta_{\text{reg}} = \infty$ and $\delta = 0$, Algorithm (5) becomes nearly equivalent to the version of the EFA-HMC method originally introduced in Ref. [148]. In practice, a good starting place for performing EFA-HMC updates is to use a trajectory length $T_t = N_t \Delta t \approx \pi/2$ with $N_t \approx 8$, $\eta_{\text{reg}} = 0.0$ and $\delta = 0.05$ [103]. If the acceptance rate is low ($\lesssim 60\%$), the first thing to try is decreasing Δt and increasing N_t such that the trajectory length T_t is held fixed. If the acceptance rate is very large ($\gtrsim 95\%$) it may be worth decreasing N_t while increasing Δt .

3.9 Reflection, Swap and Radial Updates

While HMC updates improve the decorrelation of phonon fields, other factors can increase the autocorrelation time. In the case of the Holstein model, the e - ph interaction induces an effective phonon mediated electron-electron attraction, giving rise to heavy bipolaron physics

Algorithm 4 EFA

Inputs: $x(t)$, $p(t)$, Δt .
 Calculate regularized harmonic frequency: $\Omega_{\text{reg}} = \sqrt{1 + \eta_{\text{reg}}^2} \Omega$.
 Fourier transform phonon fields: $\tilde{x}(t) = \mathcal{F} \cdot x(t)$.
 Fourier transform conjugate momentum: $\tilde{p}(t) = \mathcal{F} \cdot p(t)$.
for $n \in [0, L_\tau - 1]$ **do**
 Calculate dynamical spring constant: $\tilde{k}_n = \Delta\tau M \Omega^2 \left[1 + \frac{4}{\Delta\tau^2 \Omega^2} \sin^2 \left(\frac{\pi n}{L_\tau} \right) \right]$.
 Calculate dynamics mass: $\tilde{M}_n = \Delta\tau M \left[1 + \frac{4}{\Delta\tau^2 \Omega_{\text{reg}}^2} \sin^2 \left(\frac{\pi n}{L_\tau} \right) \right]$.
 Calculate dynamical harmonic frequency: $\tilde{\omega}_n = \sqrt{\tilde{k}_n / \tilde{M}_n}$.
 Evolve phonon fields: $\tilde{x}_n(t + \Delta t) = \tilde{x}_n(t) \cos(\tilde{\omega}_n \Delta t) + \tilde{p}_n \sin(\tilde{\omega}_n \Delta t) / (\tilde{M}_n \tilde{\omega}_n)$.
 Evolve conjugate momentum: $\tilde{p}_n(t + \Delta t) = \tilde{p}_n(t) \cos(\tilde{\omega}_n \Delta t) - \tilde{x}_n \sin(\tilde{\omega}_n \Delta t) \times (\tilde{M}_n \tilde{\omega}_n)$.
end for
 Inverse Fourier transform conjugate momentum: $p(t + \Delta t) = \mathcal{F}^\dagger \cdot \tilde{p}(t + \Delta t)$.
 Inverse Fourier transform phonon fields: $x(t + \Delta t) = \mathcal{F}^\dagger \cdot \tilde{x}(t + \Delta t)$.
Output: $x(t + \Delta t)$, $p(t + \Delta t)$.

at moderate to large coupling, also resulting in long autocorrelation times. Likewise, DQMC simulations of the repulsive Hubbard with strong interactions ($U/t \gg 1$) contend with low acceptance rates for local updates as the HS fields develop a tendency to align in the imaginary time direction [150].

Another potential issue that can arise is a formal ergodicity problem if only HMC updates are used to sample the phonon fields. In particular, the Fermion determinant $\det M_\sigma$ going to zero corresponds to the action $S(x)$ diverging. Thus, contours of $\det M_\sigma = 0$ in the phonon configuration phase space describe nodal surfaces that separate regions of $\det M_\sigma > 0$ and $\det M_\sigma < 0$ by an infinite potential energy barrier $S(x) \rightarrow \infty$. A typical HMC update cannot cross these surfaces [101, 151], which introduces a formal ergodicity problem that is both difficult to predict *a priori* and challenging to diagnose. There is no general guarantee that prevents this from occurring, and the issue has been observed in simulations of *e*-*ph* models in the anti-adiabatic limit ($\Omega/t \geq 1$) [147].

For these reasons, `SmoQyDQMC.jl` includes three additional types of updates, termed reflection, swap and radial updates. In the case of a reflection update, the phonon fields of a randomly chosen phonon mode in the lattice are reflected about the origin for all imaginary times simultaneously. In a swap update, two phonon modes in the lattice are randomly chosen, and their phonon fields are interchanged, or “swapped,” for all imaginary-time slices [102]. Similar updates can be used for the discrete HS fields which decouple the Hubbard interaction [150]. The utility of these types of updates lies in the fact that they propose large, discontinuous changes to multiple degrees of freedom simultaneously, allowing simulations to cross regions of phase space that would otherwise be inaccessible using smaller, incremental updates.

Lastly, phonon field configurations can also be updated using the recently introduced radial update [152, 153]. Here, the phonon fields are all multiplied by a random factor sampled from a lognormal distribution. The update is then accepted or rejected using a modified Metropolis-Hastings rule. Radial updates allow for discontinuous changes to every phonon degree of freedom simultaneously while retaining a high acceptance rate even as the system size is increased. In Ref. [153], introducing radial updates was shown to resolve ergodicity issues in Hubbard model DQMC simulations with continuous Gaussian HS fields sampled via HMC updates, in which the ergodicity breaking originates from nodal boundaries of the type described above.

Algorithm 5 EFA-HMC

Input: x , Δt , N_t , δ .
 Randomize time-step: $\Delta t := [1 + \text{Uniform}(-\delta, \delta)] \times \Delta t$.
 Record initial phonon configuration: $x_i := x$.
 Sample a vector of standard normal random numbers: $R \sim N(0, 1)$.
 Initialize momentum p using Eq. (84): $p := \sqrt{\mathcal{M}}R$.
 Calculate initial energy: $H_i := S(x_i) + \frac{1}{2}p^T \mathcal{M}p$.
for $t \in [1, N_t]$ **do**
 Apply algorithm (4): $(x, p) := \text{EFA}(x, p, \Delta t/2)$.
 Calculate relevant force: $f := -\left(\frac{\partial S}{\partial x} - \frac{\partial S_{\text{qho}}}{\partial x}\right)$.
 Update the momentum: $p := p + \Delta t \cdot f$.
 Apply algorithm (4): $(x, p) := \text{EFA}(x, p, \Delta t/2)$.
end for
 Calculate final energy: $H_f := S(x_f) + \frac{1}{2}p_f^T \mathcal{M}p_f$.
 Calculate change in energy: $\Delta H := H_f - H_i$.
 Calculate acceptance probability: $P := \min(1, e^{-\Delta H})$.
 Sample $r \sim \text{Uniform}(0, 1)$.
if $r < P$ **then**
 Accept final phonon configuration: $x := x_f$.
else
 Revert to initial phonon configuration: $x := x_i$.
end if
Output: x .

3.10 Error Estimation and Reweighting

This section will review how `SmoQyDQMC.jl` computes the error associated with measured observables using the binning method and how the sign problem is addressed with reweighting [154] and the Jackknife algorithm [19].

To reliably calculate the error associated with the sample mean for a measured observable, effectively independent samples are required. However, the sequence of states generated by Markov chain Monte Carlo (MCMC) algorithms like DQMC is highly correlated. A standard approach to addressing this issue is the binning, or blocking method [19]. In this approach, the sequence of measurements generated in a MCMC simulation is partitioned into equally sized bins, or intervals, and the average value is computed for each bin. Once the bins become sufficiently large, containing a number of sequential measurements larger than the autocorrelation time, the average values associated with each bin may be treated as statistically independent samples. To calculate the error, one then calculates the sample standard deviation of the mean associated with the binned averages.

Version 2.0 of `SmoQyDQMC.jl` introduces several changes to how I/O is structured within a given simulations. A DQMC simulation using the current version of `SmoQyDQMC.jl` is structured such that N_{meas} measurements are made during the simulation, which are aggregated and written to HDF5 file N_{bins} times using the `HDF5.jl` package [155]. Therefore, each set of measurements written to file is the average of $N_{\text{binsize}} = (N_{\text{meas}}/N_{\text{bins}})$ individual measurements, where it is assumed that $\text{mod}(N_{\text{meas}}, N_{\text{bins}}) = 0$. Once the simulation is complete, and as long as the binary data files persist, the mean and error for any measurement can be calculated using n_{bins} bins, where $n_{\text{bins}} \leq N_{\text{bins}}$ and $\text{mod}(N_{\text{bins}}, n_{\text{bins}}) = 0$. Note, `SmoQyDQMC.jl` 2.0 simulations can also be configured to hold all the binned data in memory during the simulation, which is useful when treating smaller systems where frequent writes to file would cause significant latency issues.

The binning method outlined above is a generic method for calculating the error associated with estimates generated by a MCMC simulation. However, the situation in a generic DQMC simulation is more complicated. The expectation value of an observable \hat{O} is given by

$$\langle O \rangle = \frac{\text{Tr} \left[e^{-\beta \hat{H}} \hat{O} \right]}{\text{Tr} \left[e^{-\beta \hat{H}} \right]}, \quad (106)$$

which is reformulated as

$$\langle O \rangle = \frac{\sum_s \int \mathcal{D}x W(s, s', x) O}{\sum_s \int \mathcal{D}x W(s, s', x)}, \quad (107)$$

where $W(s, s', x)$ is defined in Eq. (36). Ideally, this expression would be directly evaluated by performing a MCMC simulation with $W(s, s', x)$ used as the Monte Carlo weights. Unfortunately, the sign problem prevents this direct approach, which manifests as $W(s, s', x)$ not remaining a strictly positive real number. As a result, `SmoQyDQMC.jl` instead uses $\bar{W}(s, s', x)$ as the Monte Carlo weight in DQMC simulations, as defined in Eq. (37). The severity of the sign problem is then characterized by the average sign $\mathcal{S} = \overline{\langle S \rangle}$, where

$$\mathcal{S} = \frac{W(s, s', x)}{\bar{W}(s, s', x)}, \quad (108)$$

and we have adopted the notation

$$\overline{\langle O \rangle} = \frac{\sum_s \int \mathcal{D}x \bar{W}(s, s', x) O}{\sum_s \int \mathcal{D}x \bar{W}(s, s', x)}. \quad (109)$$

In the absence of a sign problem, $\mathcal{S} = 1$. The sign problem then becomes progressively worse as \mathcal{S} approaches zero. The origin and behavior of the sign problem is not entirely understood, but it is known to be particularly sensitive to increasing the system size, inverse temperature, and Hubbard interaction strength [121].

In this scenario, the reweighting method is used to extract the correct expectation value for an given observable according to

$$\langle O \rangle = \overline{\langle OS \rangle} / \overline{\langle S \rangle} = \overline{\langle OS \rangle} / \mathcal{S}. \quad (110)$$

At this point the Jackknife algorithm is used to correctly propagate errors. The Jackknife algorithm is a method for evaluating functions of expectation values, as in Eq. (110), and is used in conjunction with the binning method. For more information, we refer the reader to Ref. [19] for a thorough description and derivation.

3.11 Chemical Potential Tuning

The DQMC method is formulated in the grand canonical ensemble, where the average charge density $\langle n \rangle$ is determined by the chemical potential μ . The `SmoQyDQMC.jl` package provides two modes of operation to control the average particle number. The first mode is the traditional approach, where the chemical potential μ is fixed during the simulation, and $\langle n \rangle$ converges to its equilibrium value. Using this approach, one typically performs several runs at different values of μ to determine the value needed to produce the desired charge density $\langle n \rangle$. The second mode automates this process, dynamically adjusting the chemical potential μ to obtain a target value for the charge density $\langle n \rangle$ specified by the user. This automation is achieved using the algorithm described in Ref. [156] and has been implemented as a stand-alone package `MuTuner.jl` [157] that `SmoQyDQMC.jl` uses to incorporate this functionality.

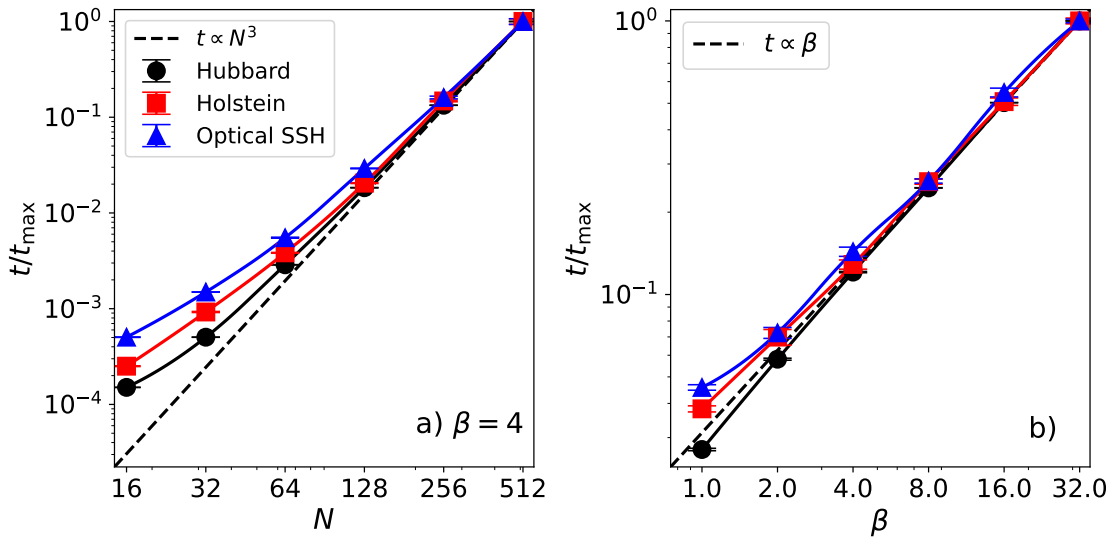


Figure 1: The average time per Monte Carlo update sweep, including the time needed for measurements of the time-displaced Green’s function, for the one-dimension (1D) Hubbard (black \circ), Holstein (red \square), and optical SSH (blue Δ) chains. The left panel plots results as a function of the chain length \mathcal{N} at a fixed $\beta = 4/t$. The right panel shows results as a function of inverse temperature β for a fixed chain length $\mathcal{N} = 256$. All results have been normalized to the largest time and the dashed line shows the ideal $O(\beta \mathcal{N}^3)$ curve.

The μ tuning algorithm can be utilized in simulations with and without a Fermion sign problem; however, we have found that the chemical potential tuning can become unstable if the average value of the Fermion sign becomes too small. When this occurs, we recommend reverting to the fixed μ mode of operation.

4 Performance

Figure 1 assesses the performance of the SmoQyDQMC.jl package for three representative models, namely the single-band Hubbard, Holstein, and optical SSH Hamiltonians, defined on 1D chains of length \mathcal{N} . The dimension of the system is unimportant with respect to measuring the scaling of the DQMC algorithm, which nominally scales as the cube of the total number of orbitals in the system \mathcal{N}^3 , independent of the dimension.

Figure 1 reports the simulation run time, including the time needed to perform measurements of the time-displaced Green’s function and normalized by the number of updates that were performed. All simulations were performed at half-filling ($\mu = 0$) with fixed $\Delta\tau = 0.1$ and adopting only nearest neighbor hopping t . For the Hubbard model, we set $U = 4t$ to place the system in the Mott insulating regime in one dimension. For the Holstein and optical SSH simulations, we set the phonon energy $\Omega = t$ and $e\text{-ph}$ coupling $\alpha = t$, giving rise to charge ordered states. We note, however, that we have obtained similar performance measures when simulating low-energy optical and acoustic phonon modes [72], which are traditionally very challenging for conventional QMC approaches [142, 143]. Finally, the asymmetric form for the propagator matrices was used in the Holstein and Hubbard simulations without the checkerboard approximation. For the simulations of the optical SSH model, we adopted the symmetric propagator definition and checkerboard approximation.

Figure 1 demonstrates that `SmoQyDQMC.jl` achieves the nominal $O(\beta \mathcal{N}^3)$ scaling of the DQMC algorithm for all three cases. This result confirms that our HMC updates for the phonon fields are efficient and bypass the typical increase in computational complexity normally associated with performing global or block updates of the phonon fields [75].

It is also straightforward to parallelize `SmoQyDQMC.jl` simulations with MPI using the `MPI.jl` package [158]. `SmoQyDQMC.jl` does not list this package as a dependency, but rather the parallelization is introduced at the script level. Examples demonstrating this functionality are included in the online [documentation](#). Additionally, when simulations are parallelized using `MPI.jl`, final estimates for measured observables are obtained by averaging results over all walkers simulated in parallel.

5 Summary & Future Directions

The `SmoQyDQMC.jl` package, implemented in the Julia programming language, exports a user-friendly implementation of the DQMC method for simulating Hubbard and e -ph interactions without sacrificing performance. By adopting a scripting interface, `SmoQyDQMC.jl` is unique relative to similar DQMC software packages, opening the door to integrating the exported functionality into more complicated workflows that leverage the growing Julia ecosystem of scientific computing and machine learning packages. With extensive [online documentation](#) that includes an ever-growing list of examples, `SmoQyDQMC.jl` will help make the DQMC method accessible to a broader community of researchers.

Moving forward, one obvious direction for future development is expanding the class of Hamiltonians that `SmoQyDQMC.jl` can simulate. Adding support for user-defined Fermion interactions, and couplings to classical degrees of freedom are all planned for future releases. Adding support for an arbitrary number of Fermion spin species, and asymmetric couplings to each spin sector is also planned. Longer term goals include developing a suite of companion packages that export other QMC variants, including the dynamical cluster approximation that uses DQMC as a solver [31, 159], linear-scaling QMC methods for simulating e -ph models [102], the zero-temperature projector QMC method [13, 124], and constrained path QMC algorithms for tackling the sign problem [37, 160].

Acknowledgments

We thank C. Miles and G. Batrouni for useful discussions and collaborations with the various algorithms utilized by this package. We also thank E. Khatami for useful feedback and advice on how to improve the file IO system in `SmoQyDQMC.jl`.

Funding information: The initial development and release of the `SmoQyDQMC.jl` package was supported by the U.S. Department of Energy, Office of Science, Office of Basic Energy Sciences, under Award Number DE-SC0022311. Improvements added in the version 2.0 release were supported by the National Science Foundation under Grant No. OAC-2410280. B.C.-S. acknowledges additional support from the Simons Foundation for ongoing support of this package.

A Supported Hubbard-Stratonovich Transformations

This appendix reviews the different HS transformations that are available in `SmoQyDQMC.jl` to decouple the local and extended Hubbard interactions. Before proceeding, it is useful to define the generic Gaussian Hubbard-Stratonovich (GHS) and Gauss-Hermite Hubbard-Stratonovich (GHHS) transformations for decoupling interactions of the form $\lambda\hat{O}^2$, where λ is the coupling constant and

$$\hat{O} = \sum_{n,m} \hat{c}_n^\dagger O_{n,m} \hat{c}_m \quad (111)$$

is a fermionic bilinear operator. The GHS transformation may be expressed as

$$e^{-\Delta\tau\lambda\hat{O}^2} = \frac{1}{\sqrt{2\pi}} \int_{-\infty}^{+\infty} ds e^{-S_{\text{ghs}}(s) - \Delta\tau\hat{V}_{\text{ghs}}(s)}, \quad (112)$$

where

$$\hat{V}_{\text{ghs}}(s) = s \sqrt{-2\lambda/\Delta\tau} \hat{O} \quad (113)$$

and

$$S_{\text{ghs}}(s) = \frac{s^2}{2}, \quad (114)$$

noting that $\sqrt{-2\lambda/\Delta\tau}$ is imaginary when $\lambda > 0$ and real when $\lambda < 0$.

The GHHS transformation approximates the GHS transformation in Eq. (112) as

$$e^{-\Delta\tau\lambda\hat{O}^2} \approx \frac{1}{4} \sum_{s=\pm 1, \pm 2} e^{-S_{\text{ghhs}}(s) - \Delta\tau\hat{V}_{\text{ghhs}}(s)} + \mathcal{O}([\Delta\tau\lambda]^4), \quad (115)$$

where the HS field s is now rendered discrete. In the above expression,

$$\hat{V}_{\text{ghhs}}(s) = \frac{s}{|s|} \sqrt{\frac{-2\lambda}{\Delta\tau} (3(1 - \sqrt{6}) + 2\sqrt{6}|s|)} \hat{O} \quad (116)$$

and

$$S_{\text{ghhs}}(s) = -\log \left(1 + \sqrt{6} \left[1 - \frac{2}{3}|s| \right] \right), \quad (117)$$

noting that the coefficient of \hat{O} in Eq. (116) is imaginary when $\lambda > 0$ and real when $\lambda < 0$ [5, 161–163].

A.1 Hubbard Interaction Hubbard-Stratonovich (HS) Transformations

Here we review the various HS transformations available for decoupling the local Hubbard interaction. Decompositions using either the spin or density channel are available, and they are all based on either the Hirsch Hubbard-Stratonovich (HHS) or GHHS transformations.

A.1.1 Hubbard Spin-Channel Hirsch HS Transformation

The local Hubbard interaction can be decoupled in `SmoQyDQMC.jl` using a spin-channel HHS transformation of the form

$$e^{-\Delta\tau U(\hat{n}_\uparrow - \frac{1}{2})(\hat{n}_\downarrow - \frac{1}{2})} = \gamma \sum_{s=\pm 1} e^{-\Delta\tau\hat{V}_{\text{hhs}}(s)}, \quad (118)$$

with

$$\hat{V}_{\text{hhs}}(s) = \alpha s(\hat{n}_\uparrow - \hat{n}_\downarrow), \quad (119)$$

where $\gamma = \frac{1}{2}e^{-\Delta\tau U/4}$ and $\alpha = \frac{1}{\Delta\tau} \cosh^{-1}(e^{\Delta\tau U/2})$ [138]. Note that α is real when $U > 0$ and imaginary when $U < 0$.

A.1.2 Hubbard Spin-Channel Gauss-Hermite HS Transformation

The local Hubbard interaction can be expressed as

$$U(\hat{n}_\uparrow - \frac{1}{2})(\hat{n}_\downarrow - \frac{1}{2}) = -\frac{U}{2}(\hat{n}_\uparrow - \hat{n}_\downarrow)^2 + \frac{U}{4}, \quad (120)$$

which can be decoupled using the GHHS transformation defined in Eq. (115) with $\hat{O} = (\hat{n}_\uparrow - \hat{n}_\downarrow)$ and $\lambda = -U/2$.

A.1.3 Hubbard Density-Channel Hirsch HS Transformation

The local Hubbard interaction can be decoupled in [SmoQyDQMC.jl](#) using a density-channel HHS transformation of the form

$$e^{-\Delta\tau U(\hat{n}_\uparrow - \frac{1}{2})(\hat{n}_\downarrow - \frac{1}{2})} = \gamma \sum_{s=\pm 1} e^{-\Delta\tau \hat{V}_{\text{hhs}}(s)} \quad (121)$$

with

$$\hat{V}_{\text{hhs}}(s) = \alpha s(\hat{n}_\uparrow + \hat{n}_\downarrow - 1), \quad (122)$$

where $\gamma = e^{\Delta\tau U/4}$ and $\alpha = \frac{1}{\Delta\tau} \cosh^{-1}(e^{-\Delta\tau U/2})$ [138]. Note that α is imaginary when $U > 0$ and real when $U < 0$.

A.1.4 Hubbard Density-Channel Gauss-Hermite HS Transformation

The local Hubbard interaction can be expressed as

$$U(\hat{n}_\uparrow - \frac{1}{2})(\hat{n}_\downarrow - \frac{1}{2}) = \frac{U}{2}(\hat{n}_\uparrow + \hat{n}_\downarrow - 1)^2 - \frac{U}{4}, \quad (123)$$

which can be decoupled using the GHHS transformation defined in Eq. (115) with $\hat{O} = (\hat{n}_\uparrow + \hat{n}_\downarrow - 1)$ and $\lambda = U/2$.

A.2 Extended Hubbard Interaction Hubbard-Stratonovich (HS) Transformations

In this section, we discuss two HS transformations for decoupling the extended Hubbard interaction

$$V(\hat{n}_i - 1)(\hat{n}_j - 1) = V \sum_{\sigma, \sigma'} (\hat{n}_{i,\sigma} - \frac{1}{2})(\hat{n}_{j,\sigma'} - \frac{1}{2}) \quad (124)$$

with $\hat{n}_i = (\hat{n}_{i,\uparrow} + \hat{n}_{i,\downarrow})$, one using the spin channel and the other the density channel.

A.2.1 Extended Hubbard Spin-Channel Hirsch HS Transformation

The extended Hubbard interaction can be decoupled in [SmoQyDQMC.jl](#) using a spin-channel HHS transformation of the form

$$e^{-\Delta\tau V \sum_{\sigma, \sigma'} (\hat{n}_{i,\sigma} - \frac{1}{2})(\hat{n}_{j,\sigma'} - \frac{1}{2})} = \prod_{\sigma, \sigma'} \left[\gamma \sum_{s_{\sigma, \sigma'} = \pm 1} e^{-\Delta\tau \hat{V}_{\text{hhs}}(s_{\sigma, \sigma'})} \right] \quad (125)$$

with

$$\hat{V}_{\text{hhs}}(s_{\sigma, \sigma'}) = \alpha s_{\sigma, \sigma'} (\hat{n}_{i,\sigma} - \hat{n}_{j,\sigma'}), \quad (126)$$

where $\gamma = \frac{1}{2} e^{-\Delta\tau V/4}$ and $\alpha = \frac{1}{\Delta\tau} \cosh^{-1}(e^{\Delta\tau V/2})$. Note that α is real when $V > 0$ and imaginary when $V < 0$ [138, 139].

A.2.2 Extended Hubbard Density-Channel Gauss-Hermite HS Transformation

The extended Hubbard interaction can be expressed as

$$V(\hat{n}_i - 1)(\hat{n}_j - 1) = \frac{V}{2}(\hat{n}_i + \hat{n}_j - 2)^2 - V(\hat{n}_{i,\uparrow} - \frac{1}{2})(\hat{n}_{i,\downarrow} - \frac{1}{2}) - V(\hat{n}_{j,\uparrow} - \frac{1}{2})(\hat{n}_{j,\downarrow} - \frac{1}{2}) - \frac{V}{2}, \quad (127)$$

where the second and third terms describe renormalization to the existing local Hubbard interactions. The first term can then be decoupled using the GHHS transformation defined in Eq. (115) by setting $\hat{O} = (\hat{n}_i + \hat{n}_j - 2)$ and $\lambda = V/2$. A nice aspect of this HS transformation is that there exist very clear criteria for when the sign problem will remain absent [140].

A.3 HS Transformation Selection Guidance

Here we provide some general guidance and advice for selecting which HS transformation to use in DQMC simulations. Depending on the Hamiltonian being simulated, the electron density, and what quantities are most important to measure precisely, certain HS transformations may outperform others [164–166]. While we provide some general advice below, it is also worth testing different HS transformations for a given model to see which one works best.

In the general case of a sign problem or phase problem, it typically advantageous to select a real-valued HS transformation over a complex-valued one, as the latter results in a phase problem that produces far noisier measurement signals. For instance, when simulating repulsive Hubbard models with a sign problem, it is reasonable to expect that the spin-channel HS transformations defined in Secs. A.1.1 and A.1.2 will outperform their density-channel counterparts defined in Secs. A.1.3 and A.1.4. This recommendation would then be inverted when simulating an attractive Hubbard model, in which case the density-channel HS transformations avoids a sign problem. Likewise, when deciding which HS transformation to use when simulating a doped model with extended Hubbard interactions, the spin-channel HS transformation defined in Sec. A.2.1 will likely work better for repulsive interactions while the density-channel one defined in Sec. A.2.2 will be better for attractive interactions.

In the absence of a sign or phase problem (as a result of some underlying symmetry), the decision on which HS transformation to use can be more subtle. For instance, when simulating a particle-hole symmetric half-filled repulsive Hubbard model, previous work has found that density-channel HS transformations that preserve SU(2) spin-symmetry result in less noisy spin-correlation measurements [164]. In contrast, spin-channel HS transformations for the same model are better when measuring density correlations and most other types of measurements [166]. Again, we recommend testing different HS transformations to see which works best in a given use case.

B Numerical Stabilization Routines

This section summarizes the numerical stabilization routines required to evaluate the various Green's function matrices in a DQMC simulation. Note that any intermediate matrix inversions are performed with an *LU* factorization with partial pivoting.

B.1 Routine for Stable Left Matrix Multiply

The routine outlined below updates an *LDR* factorization from $F = LDR$ to $F' = L'D'R'$ when left multiplied by a matrix U :

$$F' = UF = \underbrace{U[LDR]}_{L_0 D_0 R_0} = \underbrace{L'_0}_{L'_0} \underbrace{D'_0}_{D'_0} \underbrace{R'_0 R}_{R'_0 R} = L'D'R'. \quad (128)$$

B.2 Routine for Stable Right Matrix Multiply

The routine outlined below updates an LDR factorization from $F = LDR$ to $F' = L'D'R'$ when right multiplied by a matrix U :

$$F' = FU = \underbrace{[L DR]U}_{L D_0 R_0} = \underbrace{L}_{L'} \underbrace{D_0}_{D'} \underbrace{R_0}_{R'} = L'D'R'. \quad (129)$$

B.3 Routine for Stable Evaluation of Eq. (41)

Below is a numerically stable routine for evaluating Eq. (41) to calculate the matrix $G_\sigma(\tau, \tau)$, where the matrices $B_\sigma(\tau, 0)$ and $B_\sigma(\beta, \tau)$ are represented by the LDR factorization $F_1 = L_1 D_1 R_1$ and $F_0 = L_0 D_0 R_0$ respectively:

$$\begin{aligned} G &= [I + F_1 F_0]^{-1} \\ &= R_0^{-1} D_{0,\max}^{-1} \underbrace{[D_{1,\max}^{-1} L_1^\dagger R_0^{-1} D_{0,\max}^{-1} + D_{1,\min} R_1 L_0 D_{0,\min}^{-1}]}_M^{-1} D_{1,\max}^{-1} L_1^\dagger \\ &= R_0^{-1} D_{0,\max}^{-1} M^{-1} D_{1,\max}^{-1} L_1^\dagger. \end{aligned} \quad (130)$$

B.4 Routine for Stable Evaluation of Eq. (43)

Below is a numerically stable routine for evaluating Eq. (43) to calculate the matrix $G_\sigma(0, 0)$, where the matrix $B_\sigma(\beta, 0)$ is represented by the LDR factorization F :

$$\begin{aligned} G &= [I + F]^{-1} \\ &= R^{-1} D_{\max}^{-1} \underbrace{[R^{-1} D_{\max}^{-1} + L D_{\min}]}_M^{-1} \\ &= R^{-1} D_{\max}^{-1} M^{-1}. \end{aligned} \quad (131)$$

B.5 Routine for Stable Evaluation of Eq. (47b) and Eq. (48b)

Below is a numerically stable routine for evaluating Eq. (47b) to calculate the matrix $G_\sigma(\tau, 0)$, where the matrices $B_\sigma(\tau, 0)$ and $B_\sigma(\beta, \tau)$ are represented by the LDR factorization $F_1 = L_1 D_1 R_1$ and $F_0 = L_0 D_0 R_0$ respectively:

$$\begin{aligned} G &= [F_1^{-1} + F_0]^{-1} \\ &= R_0^{-1} D_{0,\max}^{-1} \underbrace{[D_{1,\max}^{-1} L_1^\dagger R_0^{-1} D_{1,\max}^{-1} + D_{1,\min} R_1 L_0 D_{0,\min}^{-1}]}_M^{-1} D_{1,\min} R_1 \\ &= R_0^{-1} D_{0,\max}^{-1} M^{-1} D_{1,\min} R_1. \end{aligned} \quad (132)$$

This same routine can be used to help evaluate Eq. (48b) to calculate the matrix $G_\sigma(0, \tau)$, except in this case $B_\sigma(\tau, 0)$ corresponds to the factorization F_0 and $B_\sigma(\beta, \tau)$ corresponds to F_1 .

References

[1] R. Blankenbecler, D. J. Scalapino and R. L. Sugar, *Monte Carlo calculations of coupled boson-fermion systems. I*, Phys. Rev. D **24**, 2278 (1981), doi:[10.1103/PhysRevD.24.2278](https://doi.org/10.1103/PhysRevD.24.2278).

[2] S. R. White, D. J. Scalapino, R. L. Sugar, E. Y. Loh, J. E. Gubernatis and R. T. Scalettar, *Numerical study of the two-dimensional Hubbard model*, Phys. Rev. B **40**, 506 (1989), doi:[10.1103/PhysRevB.40.506](https://doi.org/10.1103/PhysRevB.40.506).

[3] M. Fishman, S. R. White and E. M. Stoudenmire, *The ITensor Software Library for Tensor Network Calculations*, SciPost Phys. Codebases p. 4 (2022), doi:[10.21468/SciPostPhysCodeb.4](https://doi.org/10.21468/SciPostPhysCodeb.4).

[4] C.-R. Lee, S. Chiesa, C. Varney, E. Khatami, Z. Bai, E. D'Azevedo, M. Jarrell, T. Maier, S. Savrasov, R. Scalettar and K. Tomko, *QUEST: Quantum electron simulation toolbox*, SciDAC 2010 (2010).

[5] F. F. Assaad, M. Bercx, F. Goth, A. Götz, J. S. Hofmann, E. Huffman, Z. Liu, F. P. Toldin, J. S. E. Portela and J. Schwab, *The ALF (Algorithms for Lattice Fermions) project release 2.4. Documentation for the auxiliary-field quantum Monte Carlo code*, SciPost Phys. Codebases pp. 1–v2.4 (2025), doi:[10.21468/SciPostPhysCodeb.1-v2.4](https://doi.org/10.21468/SciPostPhysCodeb.1-v2.4).

[6] T. Degrand and C. DeTar, *Lattice Methods for Quantum Chromodynamics*, World Scientific, doi:<https://doi.org/10.1142/6065> (2006).

[7] B. Joó, C. Jung, N. H. Christ, W. Detmold, R. G. Edwards, M. Savage and P. Shanahan, *Status and future perspectives for lattice gauge theory calculations to the exascale and beyond*, The European Physical Journal A **55**(11), 199 (2019), doi:<https://doi.org/10.1140/epja/i2019-12919-7>.

[8] J. Carlson, S. Gandolfi, F. Pederiva, S. C. Pieper, R. Schiavilla, K. Schmidt and R. Wiringa, *Quantum Monte Carlo methods for nuclear physics*, Rev. Mod. Phys. **87**, 1067 (2015), doi:[10.1103/RevModPhys.87.1067](https://doi.org/10.1103/RevModPhys.87.1067).

[9] J. E. Lynn, I. Tews, S. Gandolfi and A. Lovato, *Quantum Monte Carlo methods in nuclear physics: recent advances*, Annual Review of Nuclear and Particle Science **69**(1), 279 (2019), doi:<https://doi.org/10.1146/annurev-nucl-101918-023600>.

[10] B. Hammond, W. Lester and P. Reynolds, *Monte Carlo Methods in Ab Initio Quantum Chemistry*, Lecture and Course Notes in Chemistry: Volume 1. World Scientific (1994).

[11] R. Needs, M. Towler, N. Drummond, P. López Ríos and J. Trail, *Variational and diffusion quantum Monte Carlo calculations with the CASINO code*, J. Chem. Phys. **152**(15), 154106 (2020), doi:[10.1063/1.5144288](https://doi.org/10.1063/1.5144288).

[12] D. Ceperley, *Path integrals in the theory of condensed Helium*, Rev. Mod. Phys. **67**, 279 (1995), doi:[10.1103/RevModPhys.67.279](https://doi.org/10.1103/RevModPhys.67.279).

[13] S. Sorella, S. Baroni, R. Car and M. Parrinello, *A novel technique for the simulation of interacting fermion systems*, Europhysics Letters **8**(7), 663 (1989), doi:[10.1209/0295-5075/8/7/014](https://doi.org/10.1209/0295-5075/8/7/014).

[14] N. Prokof'ev, B. Svistunov and I. Tupitsyn, *“Worm” algorithm in quantum Monte Carlo simulations*, Physics Letters A **238**(4), 253 (1998), doi:[https://doi.org/10.1016/S0375-9601\(97\)00957-2](https://doi.org/10.1016/S0375-9601(97)00957-2).

[15] H. G. Evertz, G. Lana and M. Marcu, *Cluster algorithm for vertex models*, Phys. Rev. Lett. **70**(7), 875 (1993), doi:[10.1103/PhysRevLett.70.875](https://doi.org/10.1103/PhysRevLett.70.875).

[16] H. G. Evertz, *The loop algorithm*, Advances in Physics **52**(1), 1 (2003), doi:<https://doi.org/10.1080/0001873021000049195>.

- [17] O. F. Syljuåsen and A. W. Sandvik, *Quantum Monte Carlo with directed loops*, Phys. Rev. E **66**, 046701 (2002), doi:[10.1103/PhysRevE.66.046701](https://doi.org/10.1103/PhysRevE.66.046701).
- [18] F. Alet, S. Wessel and M. Troyer, *Generalized directed loop method for quantum Monte Carlo simulations*, Phys. Rev. E **71**, 036706 (2005), doi:[10.1103/PhysRevE.71.036706](https://doi.org/10.1103/PhysRevE.71.036706).
- [19] J. Gubernatis, N. Kawashima and P. Werner, *Quantum Monte Carlo methods: algorithms for lattice models*, Cambridge University Press, doi:[10.1017/CBO9780511902581](https://doi.org/10.1017/CBO9780511902581) (2016).
- [20] F. Becca and S. Sorella, *Quantum Monte Carlo approaches for correlated systems*, Cambridge University Press, doi:[10.1017/9781316417041](https://doi.org/10.1017/9781316417041) (2017).
- [21] V. G. Rousseau, *Stochastic Green function algorithm*, Phys. Rev. E **77**, 056705 (2008), doi:[10.1103/PhysRevE.77.056705](https://doi.org/10.1103/PhysRevE.77.056705).
- [22] S. M. A. Rombouts, K. Van Houcke and L. Pollet, *Loop updates for quantum Monte Carlo simulations in the canonical ensemble*, Phys. Rev. Lett. **96**, 180603 (2006), doi:[10.1103/PhysRevLett.96.180603](https://doi.org/10.1103/PhysRevLett.96.180603).
- [23] K. Van Houcke, S. M. A. Rombouts and L. Pollet, *Quantum Monte Carlo simulation in the canonical ensemble at finite temperature*, Phys. Rev. E **73**, 056703 (2006), doi:[10.1103/PhysRevE.73.056703](https://doi.org/10.1103/PhysRevE.73.056703).
- [24] N. Kawashima, J. E. Gubernatis and H. G. Evertz, *Loop algorithms for quantum simulations of fermion models on lattices*, Phys. Rev. B **50**, 136 (1994), doi:[10.1103/PhysRevB.50.136](https://doi.org/10.1103/PhysRevB.50.136).
- [25] B. Beard and U.-J. Wiese, *Simulations of discrete quantum systems in continuous Euclidean time*, Phys. Rev. Lett. **77**, 5130 (1996), doi:[10.1103/PhysRevLett.77.5130](https://doi.org/10.1103/PhysRevLett.77.5130).
- [26] N. V. Prokof'ev, B. V. Svistunov and I. S. Tupitsyn, *Exact quantum Monte Carlo process for the statistics of discrete systems*, Journal of Experimental and Theoretical Physics Letters **64**(12), 911 (1996), doi:[10.1134/1.567243](https://doi.org/10.1134/1.567243).
- [27] N. V. Prokof'ev, B. V. Svistunov and I. S. Tupitsyn, *Exact, complete, and universal continuous-time worldline Monte Carlo approach to the statistics of discrete quantum systems*, Journal of Experimental and Theoretical Physics **87**(2), 310 (1998), doi:[10.1134/1.558661](https://doi.org/10.1134/1.558661).
- [28] H. Rieger and N. Kawashima, *Application of a continuous time cluster algorithm to the two-dimensional random quantum Ising ferromagnet*, The European Physical Journal B - Condensed Matter and Complex Systems **9**(2), 233 (1999), doi:[10.1007/s100510050761](https://doi.org/10.1007/s100510050761).
- [29] A. Georges and G. Kotliar, *Hubbard model in infinite dimensions*, Phys. Rev. B **45**, 6479 (1992), doi:[10.1103/PhysRevB.45.6479](https://doi.org/10.1103/PhysRevB.45.6479).
- [30] A. Georges, G. Kotliar, W. Krauth and M. J. Rozenberg, *Dynamical mean-field theory of strongly correlated fermion systems and the limit of infinite dimensions*, Rev. Mod. Phys. **68**, 13 (1996), doi:[10.1103/RevModPhys.68.13](https://doi.org/10.1103/RevModPhys.68.13).
- [31] T. Maier, M. Jarrell, T. Pruschke and M. H. Hettler, *Quantum cluster theories*, Rev. Mod. Phys. **77**, 1027 (2005), doi:[10.1103/RevModPhys.77.1027](https://doi.org/10.1103/RevModPhys.77.1027).

[32] M. Jarrell, *Hubbard model in infinite dimensions: A quantum Monte Carlo study*, Phys. Rev. Lett. **69**, 168 (1992), doi:[10.1103/PhysRevLett.69.168](https://doi.org/10.1103/PhysRevLett.69.168).

[33] M. Jarrell, T. Maier, C. Huscroft and S. Moukouri, *Quantum Monte Carlo algorithm for nonlocal corrections to the dynamical mean-field approximation*, Phys. Rev. B **64**, 195130 (2001), doi:[10.1103/PhysRevB.64.195130](https://doi.org/10.1103/PhysRevB.64.195130).

[34] J. E. Gubernatis, M. Jarrell, R. N. Silver and D. S. Sivia, *Quantum Monte Carlo simulations and maximum entropy: Dynamics from imaginary-time data*, Phys. Rev. B **44**, 6011 (1991), doi:[10.1103/PhysRevB.44.6011](https://doi.org/10.1103/PhysRevB.44.6011).

[35] M. Jarrell and J. E. Gubernatis, *Bayesian inference and the analytic continuation of imaginary-time quantum Monte Carlo data*, Physics Reports **269**(3), 133 (1996), doi:[10.1016/0370-1573\(95\)00074-7](https://doi.org/10.1016/0370-1573(95)00074-7).

[36] A. W. Sandvik, *Stochastic series expansion method with operator-loop update*, Phys. Rev. B **59**, R14157 (1999), doi:[10.1103/PhysRevB.59.R14157](https://doi.org/10.1103/PhysRevB.59.R14157).

[37] S. Zhang, J. Carlson and J. E. Gubernatis, *Constrained path Monte Carlo method for fermion ground states*, Phys. Rev. B **55**, 7464 (1997), doi:[10.1103/PhysRevB.55.7464](https://doi.org/10.1103/PhysRevB.55.7464).

[38] E. Kozik, K. Van Houcke, E. Gull, L. Pollet, N. Prokof'ev, B. Svistunov and M. Troyer, *Diagrammatic Monte Carlo for correlated fermions*, EPL (Europhysics Letters) **90**(1), 10004 (2010), doi:[10.1209/0295-5075/90/10004](https://doi.org/10.1209/0295-5075/90/10004).

[39] E. Kozik, E. Burovski, V. W. Scarola and M. Troyer, *Néel temperature and thermodynamics of the half-filled three-dimensional Hubbard model by diagrammatic determinant Monte Carlo*, Phys. Rev. B **87**, 205102 (2013), doi:[10.1103/PhysRevB.87.205102](https://doi.org/10.1103/PhysRevB.87.205102).

[40] E. Gull, P. Staar, S. Fuchs, P. Nukala, M. S. Summers, T. Pruschke, T. C. Schulthess and T. Maier, *Submatrix updates for the continuous-time auxiliary-field algorithm*, Phys. Rev. B **83**(7), 075122 (2011), doi:[10.1103/PhysRevB.83.075122](https://doi.org/10.1103/PhysRevB.83.075122).

[41] P. K. V. V. Nukala, T. A. Maier, M. S. Summers, G. Alvarez and T. C. Schulthess, *Fast update algorithm for the quantum Monte Carlo simulation of the Hubbard model*, Phys. Rev. B **80**, 195111 (2009), doi:[10.1103/PhysRevB.80.195111](https://doi.org/10.1103/PhysRevB.80.195111).

[42] E. Gull, M. Ferrero, O. Parcollet, A. Georges and A. J. Millis, *Momentum-space anisotropy and pseudogaps: A comparative cluster dynamical mean-field analysis of the doping-driven metal-insulator transition in the two-dimensional Hubbard model*, Phys. Rev. B **82**(15), 155101 (2010), doi:[10.1103/PhysRevB.82.155101](https://doi.org/10.1103/PhysRevB.82.155101).

[43] J. E. Hirsch, *Two-dimensional Hubbard model: Numerical simulation study*, Phys. Rev. B **31**, 4403 (1985), doi:[10.1103/PhysRevB.31.4403](https://doi.org/10.1103/PhysRevB.31.4403).

[44] B. Moritz, F. Schmitt, W. Meevasana, S. Johnston, E. M. Motoyama, M. Greven, D. H. Lu, C. Kim, R. T. Scalettar, Z.-X. Shen and T. P. Devereaux, *Effect of strong correlations on the high energy anomaly in hole- and electron-doped high- T_c superconductors*, New Journal of Physics **11**(9), 093020 (2009), doi:[10.1088/1367-2630/11/9/093020](https://doi.org/10.1088/1367-2630/11/9/093020).

[45] Z. Meng, S. Wessel, A. Muramatsu, T. Lang and F. Assaad, *Quantum spin liquid emerging in two-dimensional correlated Dirac fermions*, Nature **464**, 847 (2010), doi:<https://doi.org/10.1038/nature08942>.

[46] S. Sorella, Y. Otsuka and S. Yunoki, *Absence of a spin liquid phase in the Hubbard model on the honeycomb lattice*, Sci. Rep. **2**, 992 (2012), doi:<https://doi.org/10.1038/srep00992>.

[47] F. F. Assaad and I. F. Herbut, *Pinning the order: The nature of quantum criticality in the Hubbard model on honeycomb lattice*, Phys. Rev. X **3**, 031010 (2013), doi:[10.1103/PhysRevX.3.031010](https://doi.org/10.1103/PhysRevX.3.031010).

[48] E. Khatami, R. T. Scalettar and R. R. P. Singh, *Finite-temperature superconducting correlations of the Hubbard model*, Phys. Rev. B **91**, 241107 (2015), doi:[10.1103/PhysRevB.91.241107](https://doi.org/10.1103/PhysRevB.91.241107).

[49] Y.-Y. He, M. Qin, H. Shi, Z.-Y. Lu and S. Zhang, *Finite-temperature auxiliary-field quantum Monte Carlo: Self-consistent constraint and systematic approach to low temperatures*, Phys. Rev. B **99**, 045108 (2019), doi:[10.1103/PhysRevB.99.045108](https://doi.org/10.1103/PhysRevB.99.045108).

[50] E. W. Huang, R. Sheppard, B. Moritz and T. P. Devereaux, *Strange metallicity in the doped Hubbard model*, Science **366**(6468), 987 (2019), doi:[10.1126/science.aau7063](https://doi.org/10.1126/science.aau7063).

[51] M. Yao, D. Wang and Q.-H. Wang, *Determinant quantum Monte Carlo for the half-filled Hubbard model with nonlocal density-density interactions*, Phys. Rev. B **106**, 195121 (2022), doi:[10.1103/PhysRevB.106.195121](https://doi.org/10.1103/PhysRevB.106.195121).

[52] R. R. d. Santos, *Introduction to quantum Monte Carlo simulations for fermionic systems*, Brazilian Journal of Physics **33**, 36 (2003), doi:<https://doi.org/10.1590/S0103-97332003000100003>.

[53] G. Dopf, A. Muramatsu and W. Hanke, *Three-band Hubbard model: A Monte Carlo study*, Phys. Rev. B **41**, 9264 (1990), doi:[10.1103/PhysRevB.41.9264](https://doi.org/10.1103/PhysRevB.41.9264).

[54] Y. F. Kung, C.-C. Chen, Y. Wang, E. W. Huang, E. A. Nowadnick, B. Moritz, R. T. Scalettar, S. Johnston and T. P. Devereaux, *Characterizing the three-orbital Hubbard model with determinant quantum Monte Carlo*, Phys. Rev. B **93**, 155166 (2016), doi:[10.1103/PhysRevB.93.155166](https://doi.org/10.1103/PhysRevB.93.155166).

[55] S. Li, N. Kaushal, Y. Wang, Y. Tang, G. Alvarez, A. Nocera, T. A. Maier, E. Dagotto and S. Johnston, *Nonlocal correlations in the orbital selective Mott phase of a one-dimensional multiorbital Hubbard model*, Phys. Rev. B **94**, 235126 (2016), doi:[10.1103/PhysRevB.94.235126](https://doi.org/10.1103/PhysRevB.94.235126).

[56] E. W. Huang, C. B. Mendl, S. Liu, S. Johnston, H.-C. Jiang, B. Moritz and T. P. Devereaux, *Numerical evidence of fluctuating stripes in the normal state of high- T_c cuprate superconductors*, Science **358**(6367), 1161 (2017), doi:[10.1126/science.aak9546](https://doi.org/10.1126/science.aak9546).

[57] Y. Liu, M. Cho and B. Rubenstein, *Ab initio finite temperature auxiliary field quantum Monte Carlo*, J. Chem. Theory Comput. **14**, 4722 (2018), doi:[10.1021/acs.jctc.8b00569](https://doi.org/10.1021/acs.jctc.8b00569).

[58] H. Hao, B. M. Rubenstein and H. Shi, *Auxiliary field quantum Monte Carlo for multiband Hubbard models: Controlling the sign and phase problems to capture Hund's physics*, Phys. Rev. B **99**, 235142 (2019), doi:[10.1103/PhysRevB.99.235142](https://doi.org/10.1103/PhysRevB.99.235142).

[59] S. Li, A. Nocera, U. Kumar and S. Johnston, *Particle-hole asymmetry in the dynamical spin and charge responses of corner-shared 1D cuprates*, Communications Physics **4**(1), 217 (2021), doi:[10.1038/s42005-021-00718-w](https://doi.org/10.1038/s42005-021-00718-w).

[60] A. Moreo and D. J. Scalapino, *Two-dimensional negative-U Hubbard model*, Phys. Rev. Lett. **66**, 946 (1991), doi:[10.1103/PhysRevLett.66.946](https://doi.org/10.1103/PhysRevLett.66.946).

[61] R. T. Scalettar, E. Y. Loh, J. E. Gubernatis, A. Moreo, S. R. White, D. J. Scalapino, R. L. Sugar and E. Dagotto, *Phase diagram of the two-dimensional negative-U Hubbard model*, Phys. Rev. Lett. **62**, 1407 (1989), doi:[10.1103/PhysRevLett.62.1407](https://doi.org/10.1103/PhysRevLett.62.1407).

[62] R. A. Fontenele, N. C. Costa, R. R. dos Santos and T. Paiva, *Two-dimensional attractive Hubbard model and the BCS-BEC crossover*, Phys. Rev. B **105**, 184502 (2022), doi:[10.1103/PhysRevB.105.184502](https://doi.org/10.1103/PhysRevB.105.184502).

[63] X. Zhu, W. Han, S. Feng and H. Guo, *Quantum Monte Carlo study of the attractive kagome-lattice Hubbard model*, Phys. Rev. Res. **5**, 023037 (2023), doi:[10.1103/PhysRevResearch.5.023037](https://doi.org/10.1103/PhysRevResearch.5.023037).

[64] R. T. Scalettar, N. E. Bickers and D. J. Scalapino, *Competition of pairing and Peierls-charge-density-wave correlations in a two-dimensional electron-phonon model*, Phys. Rev. B **40**, 197 (1989), doi:[10.1103/PhysRevB.40.197](https://doi.org/10.1103/PhysRevB.40.197).

[65] I. Esterlis, B. Nosarzewski, E. W. Huang, B. Moritz, T. P. Devereaux, D. J. Scalapino and S. A. Kivelson, *Breakdown of the Migdal-Eliashberg theory: A determinant quantum Monte Carlo study*, Phys. Rev. B **97**, 140501 (2018), doi:[10.1103/PhysRevB.97.140501](https://doi.org/10.1103/PhysRevB.97.140501).

[66] O. Bradley, G. G. Batrouni and R. T. Scalettar, *Superconductivity and charge density wave order in the two-dimensional Holstein model*, Phys. Rev. B **103**, 235104 (2021), doi:[10.1103/PhysRevB.103.235104](https://doi.org/10.1103/PhysRevB.103.235104).

[67] B. Cohen-Stead, K. Barros, Z. Meng, C. Chen, R. T. Scalettar and G. G. Batrouni, *Langevin simulations of the half-filled cubic Holstein model*, Phys. Rev. B **102**, 161108 (2020), doi:[10.1103/PhysRevB.102.161108](https://doi.org/10.1103/PhysRevB.102.161108).

[68] P. M. Dee, J. Coulter, K. G. Kleiner and S. Johnston, *Relative importance of nonlinear electron-phonon coupling and vertex corrections in the Holstein model*, Communications Physics **3**(1), 145 (2020), doi:[10.1038/s42005-020-00413-2](https://doi.org/10.1038/s42005-020-00413-2).

[69] S. Li and S. Johnston, *Quantum Monte Carlo study of lattice polarons in the two-dimensional three-orbital Su-Schrieffer-Heeger model*, npj Quantum Materials **5**(1), 40 (2020), doi:[10.1038/s41535-020-0243-3](https://doi.org/10.1038/s41535-020-0243-3).

[70] B. Xing, W.-T. Chiu, D. Poletti, R. T. Scalettar and G. Batrouni, *Quantum Monte Carlo simulations of the 2D Su-Schrieffer-Heeger model*, Phys. Rev. Lett. **126**, 017601 (2021), doi:[10.1103/PhysRevLett.126.017601](https://doi.org/10.1103/PhysRevLett.126.017601).

[71] B. Cohen-Stead, K. Barros, R. Scalettar and S. Johnston, *A hybrid Monte Carlo study of bond-stretching electron-phonon interactions and charge order in BaBiO₃*, npj Computational Materials **9**(1), 40 (2023), doi:[10.1038/s41524-023-00998-6](https://doi.org/10.1038/s41524-023-00998-6).

[72] S. Malkaruge Costa, B. Cohen-Stead, A. Tanjaroon Ly, J. Neuhaus and S. Johnston, *Comparative determinant quantum Monte Carlo study of the acoustic and optical variants of the Su-Schrieffer-Heeger model*, Phys. Rev. B **108**, 165138 (2023), doi:[10.1103/PhysRevB.108.165138](https://doi.org/10.1103/PhysRevB.108.165138).

[73] A. Tanjaroon Ly, B. Cohen-Stead, S. Malkaruge Costa and S. Johnston, *Comparative study of the superconductivity in the Holstein and optical Su-Schrieffer-Heeger models*, Phys. Rev. B **108**, 184501 (2023), doi:[10.1103/PhysRevB.108.184501](https://doi.org/10.1103/PhysRevB.108.184501).

[74] X. Cai, Z.-X. Li and H. Yao, *High-temperature superconductivity induced by the Su-Schrieffer-Heeger electron-phonon coupling*, Phys. Rev. B **112**, 144517 (2025), doi:[10.1103/rhss-d52m](https://doi.org/10.1103/rhss-d52m).

[75] S. Johnston, E. A. Nowadnick, Y. F. Kung, B. Moritz, R. T. Scalettar and T. P. Devereaux, *Determinant quantum Monte Carlo study of the two-dimensional single-band Hubbard-Holstein model*, Phys. Rev. B **87**, 235133 (2013), doi:[10.1103/PhysRevB.87.235133](https://doi.org/10.1103/PhysRevB.87.235133).

[76] N. C. Costa, K. Seki, S. Yunoki and S. Sorella, *Phase diagram of the two-dimensional Hubbard-Holstein model*, Communications Physics **3**, 80 (2020), doi:[10.1038/s42005-020-0342-2](https://doi.org/10.1038/s42005-020-0342-2).

[77] S. Karakuzu, A. Tanjaroon Ly, P. Mai, J. Neuhaus, T. A. Maier and S. Johnston, *Stripe correlations in the two-dimensional Hubbard-Holstein model*, Communications Physics **5**, 311 (2022), doi:[10.1038/s42005-022-01092-x](https://doi.org/10.1038/s42005-022-01092-x).

[78] C. Feng, B. Xing, D. Poletti, R. Scalettar and G. Batrouni, *Phase diagram of the Su-Schrieffer-Heeger-Hubbard model on a square lattice*, Phys. Rev. B **106**, L081114 (2022), doi:[10.1103/PhysRevB.106.L081114](https://doi.org/10.1103/PhysRevB.106.L081114).

[79] C. Feng and R. T. Scalettar, *Interplay of flat electronic bands with Holstein phonons*, Phys. Rev. B **102**, 235152 (2020), doi:[10.1103/PhysRevB.102.235152](https://doi.org/10.1103/PhysRevB.102.235152).

[80] P. Mai, B. E. Feldman and P. W. Phillips, *Topological Mott insulator at quarter filling in the interacting Haldane model*, Phys. Rev. Res. **5**, 013162 (2023), doi:[10.1103/PhysRevResearch.5.013162](https://doi.org/10.1103/PhysRevResearch.5.013162).

[81] Y. Zhong, Q. Wang, Y. Liu, H.-F. Song, K. Liu and H.-G. Luo, *Finite temperature physics of 1D topological Kondo insulator: Stable Haldane phase, emergent energy scale and beyond*, Frontiers of Physics **14**(2), 23602 (2018), doi:[10.1007/s11467-018-0868-x](https://doi.org/10.1007/s11467-018-0868-x).

[82] Y. Huang, H. Guo, J. Maciejko, R. T. Scalettar and S. Feng, *Antiferromagnetic transitions of Dirac fermions in three dimensions*, Phys. Rev. B **102**, 155152 (2020), doi:[10.1103/PhysRevB.102.155152](https://doi.org/10.1103/PhysRevB.102.155152).

[83] Y. Da Liao, J. Kang, C. N. Breiø, X. Y. Xu, H.-Q. Wu, B. M. Andersen, R. M. Fernandes and Z. Y. Meng, *Correlation-induced insulating topological phases at charge neutrality in twisted bilayer graphene*, Phys. Rev. X **11**, 011014 (2021), doi:[10.1103/PhysRevX.11.011014](https://doi.org/10.1103/PhysRevX.11.011014).

[84] Z.-X. Li, Y.-F. Jiang and H. Yao, *Majorana-time-reversal symmetries: A fundamental principle for sign-problem-free quantum Monte Carlo simulations*, Phys. Rev. Lett. **117**, 267002 (2016), doi:[10.1103/PhysRevLett.117.267002](https://doi.org/10.1103/PhysRevLett.117.267002).

[85] T. Paiva, Y. L. Loh, M. Randeria, R. T. Scalettar and N. Trivedi, *Fermions in 3D optical lattices: Cooling protocol to obtain antiferromagnetism*, Phys. Rev. Lett. **107**, 086401 (2011), doi:[10.1103/PhysRevLett.107.086401](https://doi.org/10.1103/PhysRevLett.107.086401).

[86] P. Brown, D. Mitra, E. Guardado-Sánchez, P. Schauss, S. Kondov, E. Khatami, T. Paiva, N. Trivedi, D. A. Huse and W. Bakr, *Spin-imbalance in a 2D Fermi-Hubbard system*, Science **357**, 1385 (2017), doi:[10.1126/science.aam7838](https://doi.org/10.1126/science.aam7838).

[87] P. M. Duarte, R. A. Hart, T.-L. Yang, X. Liu, T. Paiva, E. Khatami, R. T. Scalettar, N. Trivedi and R. G. Hulet, *Compressibility of a fermionic Mott insulator of ultracold atoms*, Phys. Rev. Lett. **114**, 070403 (2015), doi:[10.1103/PhysRevLett.114.070403](https://doi.org/10.1103/PhysRevLett.114.070403).

[88] R. A. Hart, P. M. Duarte, T.-L. Yang, X. Liu, T. Paiva, E. Khatami, R. T. Scalettar, N. Trivedi, D. A. Huse and R. G. Hulet, *Observation of antiferromagnetic correlations in the Hubbard model with ultracold atoms*, *Nature* **519**(7542), 211 (2015), doi:[10.1038/nature14223](https://doi.org/10.1038/nature14223).

[89] A. Masurenko, C. S. Chiu, G. Ji, M. F. Parsons, M. Kanász-Nagy, R. Schmidt, F. Grusdt, E. Demler, D. Greif and M. Greiner, *A cold-atom Fermi-Hubbard antiferromagnet*, *Nature* **545**(7655), 462 (2017), doi:[10.1038/nature22362](https://doi.org/10.1038/nature22362).

[90] M. Gall, N. Wurz, J. Samland, C. F. Chan and M. Köhl, *Competing magnetic orders in a bilayer Hubbard model with ultracold atoms*, *Nature* **589**(7840), 40 (2021), doi:[10.1038/s41586-020-03058-x](https://doi.org/10.1038/s41586-020-03058-x).

[91] T. Grover, *Quantum entanglement of interacting fermions in Monte Carlo*, *Phys. Rev. Lett.* **111**, 130402 (2013), doi:<https://doi.org/10.1103/PhysRevLett.111.130402>.

[92] F. F. Assaad, T. C. Lang and F. P. Toldin, *Entanglement spectra of interacting fermions in quantum Monte Carlo simulations*, *Phys. Rev. B* **89**(12), 125121 (2014), doi:<https://doi.org/10.1103/PhysRevB.89.125121>.

[93] P. Broecker and S. Trebst, *Entanglement and the fermion sign problem in auxiliary field quantum Monte Carlo simulations*, *Phys. Rev. B* **94**(7), 075144 (2016), doi:<https://doi.org/10.1103/PhysRevB.94.075114>.

[94] C. Wu, *Hidden symmetry and quantum phases in spin-3/2 cold atomic systems*, *Modern Physics Letters B* **20**(27), 1707 (2006), doi:[10.1142/S0217984906012213](https://doi.org/10.1142/S0217984906012213).

[95] G. Pasqualetti, O. Bettermann, N. Darkwah Oppong, E. Ibarra-García-Padilla, S. Dasgupta, R. T. Scalettar, K. R. A. Hazzard, I. Bloch and S. Fölling, *Equation of state and thermometry of the 2D SU(N) Fermi-Hubbard model*, *Phys. Rev. Lett.* **132**, 083401 (2024), doi:[10.1103/PhysRevLett.132.083401](https://doi.org/10.1103/PhysRevLett.132.083401).

[96] E. Ibarra-García-Padilla, C. Feng, G. Pasqualetti, S. Fölling, R. T. Scalettar, E. Khatami and K. R. A. Hazzard, *Metal-insulator transition and magnetism of SU(3) fermions in the square lattice*, *Phys. Rev. A* **108**, 053312 (2023), doi:[10.1103/PhysRevA.108.053312](https://doi.org/10.1103/PhysRevA.108.053312).

[97] C. Feng, E. Ibarra-García-Padilla, K. R. A. Hazzard, R. Scalettar, S. Zhang and E. Vitali, *Metal-insulator transition and quantum magnetism in the SU(3) Fermi-Hubbard model*, *Phys. Rev. Res.* **5**, 043267 (2023), doi:[10.1103/PhysRevResearch.5.043267](https://doi.org/10.1103/PhysRevResearch.5.043267).

[98] *pyALF*, <https://git.physik.uni-wuerzburg.de/ALF/pyALF>.

[99] R. T. Scalettar, D. Scalapino and R. Sugar, *New algorithm for the numerical simulation of fermions*, *Physical Review B* **34**(11), 7911 (1986), doi:<https://doi.org/10.1103/PhysRevB.34.7911>.

[100] S. Duane, A. Kennedy, B. J. Pendleton and D. Roweth, *Hybrid Monte Carlo*, *Physics Letters B* **195**, 216 (1987), doi:[https://doi.org/10.1016/0370-2693\(87\)91197-X](https://doi.org/10.1016/0370-2693(87)91197-X).

[101] S. Beyl, F. Goth and F. F. Assaad, *Revisiting the hybrid quantum Monte Carlo method for Hubbard and electron-phonon models*, *Phys. Rev. B* **97**, 085144 (2018), doi:[10.1103/PhysRevB.97.085144](https://doi.org/10.1103/PhysRevB.97.085144).

[102] B. Cohen-Stead, O. Bradley, C. Miles, G. Batrouni, R. Scalettar and K. Barros, *Fast and scalable quantum Monte Carlo simulations of electron-phonon models*, *Phys. Rev. E* **105**, 065302 (2022), doi:[10.1103/PhysRevE.105.065302](https://doi.org/10.1103/PhysRevE.105.065302).

[103] J. Ostmeyer and P. Buividovich, *Minimal autocorrelation in hybrid Monte Carlo simulations using exact fourier acceleration*, Computer Physics Communications p. 109624 (2025).

[104] S. Johnston, E. Khatami and R. Scalettar, *A perspective on machine learning and data science for strongly correlated electron problems*, Carbon Trends **9**, 100231 (2022), doi:<https://doi.org/10.1016/j.cartre.2022.100231>.

[105] G. Issa, O. Bradley, E. Khatami and R. Scalettar, *Learning by confusion: The phase diagram of the Holstein model*, Phys. Rev. B **111**, 155140 (2025), doi:[10.1103/PhysRevB.111.155140](https://doi.org/10.1103/PhysRevB.111.155140).

[106] C. Jordan, G. Issa, E. Khatami, R. Scalettar, B. Cohen-Stead and S. Johnston, *Charge order in the half-filled bond-Holstein model*, arXiv:2601.13121 (2026).

[107] *SmoQy Suite*, <https://github.com/SmoQySuite>.

[108] *Documentation for SmoQyDQMC.jl.*, <https://smoqysuite.github.io/SmoQyDQMC.jl/dev/>.

[109] *JDQMCFramework.jl*, <https://github.com/SmoQySuite/JDQMCFramework.jl>.

[110] *JDQMCMeasurements.jl*, <https://github.com/127SmoQySuite/JDQMCMeasurements.jl>.

[111] S. Barišić, J. Labbé and J. Friedel, *Tight binding and transition-metal superconductivity*, Phys. Rev. Lett. **25**, 919 (1970), doi:[10.1103/PhysRevLett.25.919](https://doi.org/10.1103/PhysRevLett.25.919).

[112] W. P. Su, J. R. Schrieffer and A. J. Heeger, *Solitons in polyacetylene*, Phys. Rev. Lett. **42**, 1698 (1979), doi:[10.1103/PhysRevLett.42.1698](https://doi.org/10.1103/PhysRevLett.42.1698).

[113] T. Holstein, *Studies of polaron motion: Part I. the molecular-crystal model*, Annals of Physics **8**(3), 325 (1959), doi:[https://doi.org/10.1016/0003-4916\(59\)90002-8](https://doi.org/10.1016/0003-4916(59)90002-8).

[114] A. S. Alexandrov and P. E. Kornilovitch, *Mobile small polaron*, Phys. Rev. Lett. **82**, 807 (1999), doi:[10.1103/PhysRevLett.82.807](https://doi.org/10.1103/PhysRevLett.82.807).

[115] M. Chakraborty, J. Chatterjee and H. Fehske, *Particularities of polaron formation in the extended Holstein model with next nearest neighbor transfer*, Phys. Rev. B **108**, 235134 (2023), doi:[10.1103/PhysRevB.108.235134](https://doi.org/10.1103/PhysRevB.108.235134).

[116] M. Capone, W. Stephan and M. Grilli, *Small-polaron formation and optical absorption in Su-Schrieffer-Heeger and Holstein models*, Phys. Rev. B **56**, 4484 (1997), doi:[10.1103/PhysRevB.56.4484](https://doi.org/10.1103/PhysRevB.56.4484).

[117] H. F. Trotter, *On the product of semi-groups of operators*, Proceedings of the American Mathematical Society **10**(4), 545 (1959), doi:[10.1090/S0002-9939-1959-0108732-6](https://doi.org/10.1090/S0002-9939-1959-0108732-6).

[118] M. Suzuki, *Relationship between d-dimensional quantal spin systems and (d + 1)-dimensional Ising systems: Equivalence, critical exponents and systematic approximants of the partition function and spin correlations*, Progress of theoretical physics **56**(5), 1454 (1976), doi:<https://doi.org/10.1143/PTP.56.1454>.

[119] C.-R. Lee, *Minimal split checkerboard method for exponentiating sparse matrices and its applications in quantum statistical mechanics*, SIAM Journal on Scientific Computing **35**, C143 (2013), doi:[10.1137/110838716](https://doi.org/10.1137/110838716).

[120] E. Y. Loh, J. E. Gubernatis, R. T. Scalettar, S. R. White, D. J. Scalapino and R. L. Sugar, *Sign problem in the numerical simulation of many-electron systems*, Phys. Rev. B **41**, 9301 (1990), doi:[10.1103/PhysRevB.41.9301](https://doi.org/10.1103/PhysRevB.41.9301).

[121] V. I. Iglovikov, E. Khatami and R. T. Scalettar, *Geometry dependence of the sign problem in quantum Monte Carlo simulations*, Phys. Rev. B **92**, 045110 (2015), doi:[10.1103/PhysRevB.92.045110](https://doi.org/10.1103/PhysRevB.92.045110).

[122] R. Mondaini, S. Tarat and R. T. Scalettar, *Quantum critical points and the sign problem*, Science **375**(6579), 418 (2022), doi:[10.1126/science.abg9299](https://doi.org/10.1126/science.abg9299).

[123] F. Assaad and H. Evertz, *World-line and determinantal quantum Monte Carlo methods for spins, phonons and electrons*, In *Computational Many-Particle Physics*, pp. 277–356. Springer, doi:[10.1007/978-3-540-74686-7_10](https://doi.org/10.1007/978-3-540-74686-7_10) (2008).

[124] G. Sugiyama and S. Koonin, *Auxiliary field Monte-Carlo for quantum many-body ground states*, Annals of Physics **168**(1), 1 (1986), doi:[https://doi.org/10.1016/0003-4916\(86\)90107-7](https://doi.org/10.1016/0003-4916(86)90107-7).

[125] E. Loh, J. Gubernatis, R. Scalettar, S. White, D. Scalapino and R. Sugar, *Numerical stability and the sign problem in the determinant quantum Monte Carlo method*, International Journal of Modern Physics C **16**(08), 1319 (2005), doi:[10.1142/S0129183105007911](https://doi.org/10.1142/S0129183105007911).

[126] Z. Bai, C. Lee, R.-C. Li and S. Xu, *Stable solutions of linear systems involving long chain of matrix multiplications*, Linear Algebra and its Applications **435**, 659 (2011), doi:<https://doi.org/10.1016/j.laa.2010.06.023>, Special Issue: Dedication to Pete Stewart on the occasion of his 70th birthday.

[127] C. Bauer, *Fast and stable determinant quantum Monte Carlo*, SciPost Phys. Core **2**, 011 (2020), doi:[10.21468/SciPostPhysCore.2.2.011](https://doi.org/10.21468/SciPostPhysCore.2.2.011).

[128] C. Bauer, *Simulating and machine learning quantum criticality in a nearly antiferromagnetic metal*, Ph.D. thesis, Universität zu Köln (2021).

[129] E. Y. Loh and J. E. Gubernatis, *Stable numerical simulations of models of interacting electrons in condensed-matter physics* **32**, 177 (1992), doi:<https://doi.org/10.1016/B978-0-444-88885-3.50009-3>.

[130] C.-R. Lee, *Minimal split checkerboard method for exponentiating sparse matrices and its applications in quantum statistical mechanics*, SIAM Journal on Scientific Computing **35**(2), C143 (2013), doi:[10.1137/110838716](https://doi.org/10.1137/110838716), <https://doi.org/10.1137/110838716>.

[131] *Checkerboard.jl*, <https://github.com/cohensbw/Checkerboard.jl>.

[132] S. Beyl, *Hybrid quantum Monte Carlo for condensed matter models*, Doctoral thesis, Universität Würzburg, doi:[10.25972/OPUS-19122](https://doi.org/10.25972/OPUS-19122) (2020).

[133] C. Gros, *Control of the finite-size corrections in exact diagonalization studies*, Phys. Rev. B **53**, 6865 (1996), doi:[10.1103/PhysRevB.53.6865](https://doi.org/10.1103/PhysRevB.53.6865).

[134] C. Lin, F. H. Zong and D. M. Ceperley, *Twist-averaged boundary conditions in continuum quantum Monte Carlo algorithms*, Phys. Rev. E **64**, 016702 (2001), doi:[10.1103/PhysRevE.64.016702](https://doi.org/10.1103/PhysRevE.64.016702).

[135] M. Qin, H. Shi and S. Zhang, *Benchmark study of the two-dimensional Hubbard model with auxiliary-field quantum Monte Carlo method*, Phys. Rev. B **94**, 085103 (2016), doi:[10.1103/PhysRevB.94.085103](https://doi.org/10.1103/PhysRevB.94.085103).

[136] S. Karakuzu, L. F. Tocchio, S. Sorella and F. Becca, *Superconductivity, charge-density waves, antiferromagnetism, and phase separation in the Hubbard-Holstein model*, Phys. Rev. B **96**, 205145 (2017), doi:[10.1103/PhysRevB.96.205145](https://doi.org/10.1103/PhysRevB.96.205145).

[137] S. Karakuzu, K. Seki and S. Sorella, *Study of the superconducting order parameter in the two-dimensional negative- U Hubbard model by grand-canonical twist-averaged boundary conditions*, Phys. Rev. B **98**, 075156 (2018), doi:[10.1103/PhysRevB.98.075156](https://doi.org/10.1103/PhysRevB.98.075156).

[138] J. E. Hirsch, *Discrete Hubbard-Stratonovich transformation for fermion lattice models*, Phys. Rev. B **28**, 4059 (1983), doi:[10.1103/PhysRevB.28.4059](https://doi.org/10.1103/PhysRevB.28.4059).

[139] L. Rademaker, S. Johnston, J. Zaanen and J. van den Brink, *Determinant quantum Monte Carlo study of exciton condensation in the bilayer Hubbard model*, Phys. Rev. B **88**, 235115 (2013), doi:[10.1103/PhysRevB.88.235115](https://doi.org/10.1103/PhysRevB.88.235115).

[140] M. Golor and S. Wessel, *Nonlocal density interactions in auxiliary-field quantum Monte Carlo simulations: Application to the square lattice bilayer and honeycomb lattice*, Phys. Rev. B **92**, 195154 (2015), doi:[10.1103/PhysRevB.92.195154](https://doi.org/10.1103/PhysRevB.92.195154).

[141] F. Sun and X. Y. Xu, *Delay update in determinant quantum Monte Carlo*, Phys. Rev. B **109**, 235140 (2024), doi:[10.1103/PhysRevB.109.235140](https://doi.org/10.1103/PhysRevB.109.235140).

[142] C. Chen, X. Y. Xu, J. Liu, G. Batrouni, R. Scalettar and Z. Y. Meng, *Symmetry-enforced self-learning Monte Carlo method applied to the Holstein model*, Phys. Rev. B **98**, 041102 (2018), doi:[10.1103/PhysRevB.98.041102](https://doi.org/10.1103/PhysRevB.98.041102).

[143] S. Li, P. M. Dee, E. Khatami and S. Johnston, *Accelerating lattice quantum Monte Carlo simulations using artificial neural networks: Application to the Holstein model*, Phys. Rev. B **100**, 020302 (2019), doi:[10.1103/PhysRevB.100.020302](https://doi.org/10.1103/PhysRevB.100.020302).

[144] G. G. Batrouni and R. T. Scalettar, *Langevin simulations of a long-range electron-phonon model*, Phys. Rev. B **99**, 035114 (2019), doi:[10.1103/PhysRevB.99.035114](https://doi.org/10.1103/PhysRevB.99.035114).

[145] R. Neal, *MCMC Using Hamiltonian Dynamics*, In S. Brooks, A. Gelman, G. Jones and X.-L. Meng, eds., *Handbook of Markov Chain Monte Carlo*, vol. 20116022. Chapman and Hall/CRC, ISBN 978-1-4200-7941-8 978-1-4200-7942-5, doi:[10.1201/b10905-6](https://doi.org/10.1201/b10905-6) (2011).

[146] G. G. Batrouni, G. R. Katz, A. S. Kronfeld, G. P. Lepage, B. Svetitsky and K. G. Wilson, *Langevin simulations of lattice field theories*, Phys. Rev. D **32**, 2736 (1985), doi:[10.1103/PhysRevD.32.2736](https://doi.org/10.1103/PhysRevD.32.2736).

[147] A. Götz, S. Beyl, M. Hohenadler and F. F. Assaad, *Valence-bond solid to antiferromagnet transition in the two-dimensional Su-Schrieffer-Heeger model by Langevin dynamics*, Phys. Rev. B **105**, 085151 (2022), doi:[10.1103/PhysRevB.105.085151](https://doi.org/10.1103/PhysRevB.105.085151).

[148] J. Ostmeyer, T. Nemataram, A. Troisi and P. Buvilovich, *First-principles quantum Monte Carlo study of charge-carrier mobility in organic molecular semiconductors*, Phys. Rev. Appl. **22**, L031004 (2024), doi:[10.1103/PhysRevApplied.22.L031004](https://doi.org/10.1103/PhysRevApplied.22.L031004).

[149] P. B. Mackenze, *An improved hybrid Monte Carlo method*, Physics Letters B **226**(3-4), 369 (1989).

[150] R. T. Scalettar, R. M. Noack and R. R. P. Singh, *Ergodicity at large couplings with the determinant Monte Carlo algorithm*, Phys. Rev. B **44**, 10502 (1991), doi:[10.1103/PhysRevB.44.10502](https://doi.org/10.1103/PhysRevB.44.10502).

[151] S. R. White and J. W. Wilkins, *Fermion simulations in systems with negative weights*, Phys. Rev. B **37**, 5024 (1988), doi:[10.1103/PhysRevB.37.5024](https://doi.org/10.1103/PhysRevB.37.5024).

[152] J. Ostmeyer, *Exponential speed up in Monte Carlo sampling through radial updates*, Journal of Physics A: Mathematical and Theoretical **58**(18), 185201 (2025).

[153] F. L. Temmen, E. Berkowitz, A. Kennedy, T. Luu, J. Ostmeyer and X. Yu, *Fully ergodic simulations using radial updates*, Phys. Rev. B **112**, 045134 (2025), doi:[10.1103/9zst-bvmk](https://doi.org/10.1103/9zst-bvmk).

[154] A. M. Ferrenberg and R. H. Swendsen, *New Monte Carlo technique for studying phase transitions*, Phys. Rev. Lett. **61**, 2635 (1988), doi:[10.1103/PhysRevLett.61.2635](https://doi.org/10.1103/PhysRevLett.61.2635).

[155] *HDF5.jl*, <https://github.com/JuliaIO/HDF5.jl.git>.

[156] C. Miles, B. Cohen-Stead, O. Bradley, S. Johnston, R. Scalettar and K. Barros, *Dynamical tuning of the chemical potential to achieve a target particle number in grand canonical Monte Carlo simulations*, Phys. Rev. E **105**, 045311 (2022), doi:[10.1103/PhysRevE.105.045311](https://doi.org/10.1103/PhysRevE.105.045311).

[157] *MuTuner.jl*, <https://github.com/cohensbw/MuTuner.jl>.

[158] S. Byrne, L. C. Wilcox and V. Churavy, *Mpi.jl: Julia bindings for the message passing interface*, Proceedings of the JuliaCon Conferences **1**(1), 68 (2021), doi:[10.21105/jcon.00068](https://doi.org/10.21105/jcon.00068).

[159] E. Khatami, C. R. Lee, Z. J. Bai, R. T. Scalettar and M. Jarrell, *Cluster solver for dynamical mean-field theory with linear scaling in inverse temperature*, Phys. Rev. E **81**, 056703 (2010), doi:[10.1103/PhysRevE.81.056703](https://doi.org/10.1103/PhysRevE.81.056703).

[160] S. Zhang, *Finite-temperature Monte Carlo calculations for systems with fermions*, Phys. Rev. Lett. **83**, 2777 (1999), doi:[10.1103/PhysRevLett.83.2777](https://doi.org/10.1103/PhysRevLett.83.2777).

[161] F. Goth, *Higher order auxiliary field quantum Monte Carlo methods*, Journal of Physics: Conference Series **2207**(1), 012029 (2022), doi:[10.1088/1742-6596/2207/1/012029](https://doi.org/10.1088/1742-6596/2207/1/012029).

[162] Y. Motome and M. Imada, *A quantum Monte Carlo method and its applications to multi-orbital Hubbard models*, Journal of the Physical Society of Japan **66**(7), 1872 (1997), doi:[10.1143/JPSJ.66.1872](https://doi.org/10.1143/JPSJ.66.1872), <https://doi.org/10.1143/JPSJ.66.1872>.

[163] F. F. Assaad, M. Imada and D. J. Scalapino, *Charge and spin structures of a $d_{x^2-y^2}$ superconductor in the proximity of an antiferromagnetic Mott insulator*, Phys. Rev. B **56**, 15001 (1997), doi:[10.1103/PhysRevB.56.15001](https://doi.org/10.1103/PhysRevB.56.15001).

[164] F. F. Assaad, *$SU(2)$ -spin invariant auxiliary field quantum Monte-Carlo algorithm for Hubbard models*, In E. Krause and W. Jäger, eds., *High Performance Computing in Science and Engineering '98*, pp. 105–111. Springer Berlin Heidelberg, Berlin, Heidelberg, ISBN 978-3-642-58600-2 (1999).

[165] H. Shi and S. Zhang, *Symmetry in auxiliary-field quantum Monte Carlo calculations*, Phys. Rev. B **88**, 125132 (2013), doi:[10.1103/PhysRevB.88.125132](https://doi.org/10.1103/PhysRevB.88.125132).

[166] *Montecarlo.jl*, <https://github.com/carstenbauer/MonteCarlo.jl.git>.